

Evolution of galaxy dynamics over the last 10 Gyrs with MUSE/VLT

Master Thesis



Author: MERCIER Wilfried

Supervisor: CONTINI Thierry

Co-Supervisor: EPINAT Benoît

Observatoire de Paris
Institut de Recherche en Astrophysique et Planétologie
Laboratoire d'Astrophysique de Marseille

July 5, 2019



Abstract

We present a morpho-kinematics study of ~ 100 star-forming galaxies located in low-density environment (so called "field" galaxies) with [OII] detection in the redshift range $0.4 < z < 1.4$ observed with MUSE, and with HST-ACS counterparts, in the COSMOS area. The main goal was to perform the kinematical modelling of a subsample of spatially resolved galaxies in an initial MUSE sample of ~ 500 galaxies at intermediate redshift in order to study the joint evolution of their morphological (size, inclination) and kinematical parameters (maximum rotation velocity and velocity dispersion) over a large range of stellar mass ($\sim 10^8 - 10^{11}$) and redshift.

In Section 1, after introducing the field of extra-galactic astrophysics and explaining the importance of morpho-kinematics analysis on the understanding of galaxy evolution through cosmic time, we give a brief overview of Integral Field Spectroscopy concept and MUSE instrument.

The methodology behind the selection of a spatially resolved sample of galaxies is given in Section 2. We retrieve from three different HST catalogues the morphological parameters of approximately half the field galaxies. We then check their consistency and robustness against each other, as well as against a morphological modelling performed by V. Abril-Melgarejo (PhD student at LAM, Marseille) on another sample of group and cluster galaxies observed in the same MUSE fields. After correcting for any bias, we select a subsample of ~ 100 spatially resolved galaxies with high enough signal-to-noise [OII] detection. According to this selection, we are losing galaxies at $z \approx 1.4$, as well as those with a low stellar mass (low size) or which are nearly quenched (low [OII] SNR).

Velocities maps based on the [OII] emission-line doublet, and produced with the CAMEL software, are automatically cleaned of pixels with fake detection and then visually inspected. Remaining isolated pixels and/or with large velocity offsets ($\approx 50 - 100 \text{ km s}^{-1}$) were also removed. We model the galaxies with a thin rotating disc using a ramp model with 3 free parameters, from which we derive inclination, beam-smearing and LSF corrected values for the maximum rotation velocity (V_{max}) and the velocity dispersion (σ_v). We give a description of the modelling in Section 3.

We provide an early investigation of the link between the morphological and kinematical properties of our sample in Section 4. The V_{max}/σ_v distribution is looked upon. We find that 90% of our sample are rotationally supported galaxies ($V_{\text{max}}/\sigma_v > 2$) and give some insight into why we have a larger proportion than in other studies. We recover the Tully-Fisher Relation and investigate its potential evolution with redshift and galaxy size. A correlation is found between SFR and velocity dispersion which seems consistent with an origin of the velocity dispersion mainly driven by energy injection during star formation.

Finally we conclude on the work accomplished during these three months and we give some indications about the next questions which will be investigated during the remaining and last month of internship at IRAP and potentially beyond if this internship is to be continued into a PhD.

Contents

1	Introduction	1
1.1	A global picture of the Universe	1
1.2	What we have learned about galaxies so far	2
1.2.1	Evolving properties with redshift ?	2
1.2.2	An impact from the environment ?	4
1.2.3	Studying the morpho-kinematical evolution of galaxies	5
1.3	Observation techniques in extra-galactic astronomy	6
1.3.1	Spectroscopy and photometry	6
1.3.2	Long slit and early integral field spectroscopy	8
1.3.3	New generation IFS with MUSE	8
2	Sample selection	10
2.1	MUSE-GTO MAGIC	10
2.2	COSMOS field	10
2.3	Prior information on the galaxies	11
2.3.1	Galaxies in structures	11
2.3.2	Morphological information from COSMOS catalogues	12
2.4	Checking catalogues values consistency	13
2.4.1	Reasons for checking catalogues values consistency and robustness	13
2.4.2	Catalogues used for comparison	14
2.4.3	Total magnitudes	14
2.4.4	Morphological type classification	16
2.4.5	Half-light radii	19
2.4.6	Ellipticity	22
2.5	SNR and size selection	23
2.5.1	Size selection	23
2.5.2	SNR selection	24
2.5.3	Inspecting galaxies	25
2.6	Characterisation of the sample	27
2.6.1	Redshift distribution	27
2.6.2	Mass-SFR relation	27
2.6.3	Morphological type	29
2.6.4	Inclination of the galaxies	29
3	Kinematical modelling	30
3.1	Velocities maps	30
3.2	Manual cleaning	30
3.3	Velocity field model	30
3.3.1	Ramp model	30
3.4	Beam-smearing and sampling effect on the dispersion	31
3.4.1	The impact of beam-smearing	31

3.4.2	Formalism for the velocity field and dispersion maps	31
3.4.3	Impact of the PSF and LSF	32
3.4.4	Spatial sampling	32
3.5	Modelling	33
4	Morpho-kinematics analysis	35
4.1	V_{\max}/σ_v distribution	35
4.2	Tully-Fisher Relation	37
4.2.1	Recovering the TFR	37
4.2.2	A size dependent relation ?	38
4.2.3	The effect of inclination	38
4.3	Scaling between SFR and velocity dispersion	39
5	Conclusion and perspectives	40
	References	41
A	PSF FWHM variation with wavelength	45
B	Additional information about kinematics	46
B.1	Velocity decomposition	46
B.2	Computing the disk scale length	46
C	Additional plots for the analysis	48
C.1	TFR	48
C.2	Effect of the inclination on the TFR	49
C.3	SFR – V_{\max} relation	50
D	Morpho-kinematics parameters of the sample	51

List of Figures

1	Rotation curves from Vera Rubin	1
2	Morphological evolution of galaxies with cosmic time	2
3	Tully-Fisher relation from MASSIV survey	5
4	Redshift distribution of the main IFS surveys	8
5	Theoretical evolution of inclination uncertainty with b/a	13
6	Comparison between GALFIT and catalogues magnitudes	15
7	Morphological types consistency	16
8	Origin of the classification discrepancy	17
9	Radii comparison between catalogues and GALFIT using bulb and disk	20
10	Radii comparison per catalogue	20
11	Half-light radius bias before/after correction	21
12	Ellipticity robustness	22
13	Sample selection	25
14	Redshift distribution	27
15	SFR-mass relation	28
16	Morphological types of the sample galaxies	29
17	Example of a kinematical model	33
18	V_{\max}/σ_v distribution	35
19	$V_{\max} - \sigma_v$ diagram as a function of apparent size	36
20	Tully-Fisher Relation	37
21	TFR as a function of galaxies physical size	38
22	Scaling between SFR and σ_v	39
23	PSF FWHM variation with wavelength.	45
24	TFR as a function of angular size	48
25	Effect of the inclination on the TFR	49
26	SFR – V_{\max} relation	50

List of Tables

1	Main characteristics of the MUSE observations in the COSMOS area.	10
2	Morpho-kinematical parameters I	51
3	Morpho-kinematical parameters II	52
4	Morpho-kinematical parameters III	53

Acknowledgements

Before beginning this report, or finishing it should I say as it is the last bit I am working on, I would like to thank a few people for the opportunity which was given to me to do my Master 2 internship at IRAP. To start with, I would like to greatly thank my two supervisors, Thierry Contini and Benoit Epinat, for their continuous support throughout this internship, for the many corrections given to the report and all the interesting discussions which followed. I would also like to thank them for letting me go to LAM, in Marseille. This stay was a great opportunity to learn more about the kinematics of galaxies observed with integral field spectroscopy while visiting during the evenings a city I had never been to until now. Also a great thank to Valentina for teaching me how to properly use all the different IDL codes and for never hesitating to answer my questions.

I obviously thank everyone who has been reading and correcting mistakes and typos in the report, starting once again with Thierry and Benoit, but also Lina Issa who has been an attentive reader during this last month. Thanks to the Observatory of Paris and IRAP for allowing me to do this internship, as well as everyone in the GAHEC group.

Finally, I more generally thank everyone I have spent time with at IRAP. The other students from the Observatory of Paris, Aline, Cyril, Naïs, Mikel and Sylvain, Segolène for spending time in the same office and for supporting with me the intense music coming from outside during the last day of the report writing, and all the other interns and PhD students we spent time with during and after lunch.

1 Introduction

1.1 A global picture of the Universe

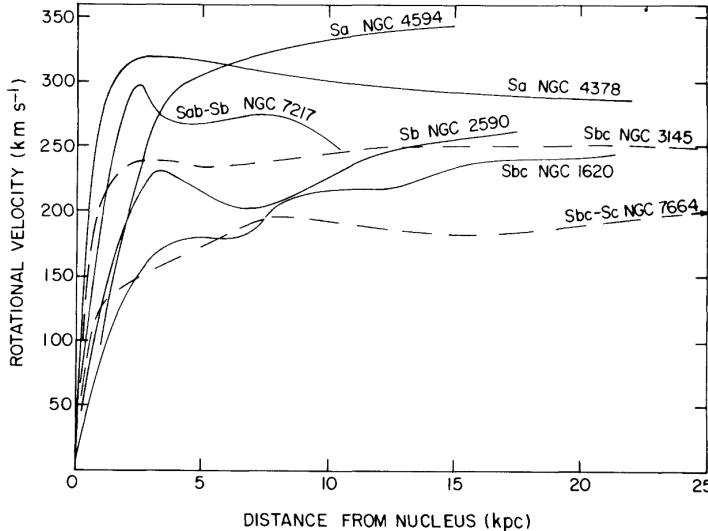


Figure 1: Rotation curves of 7 spiral galaxies observed by Vera C. Rubin, W. Kent Ford, Jr, and Norbert Thonnard (Rubin et al., 1978). These were among the first measurements which unveiled the presence of dark matter around galaxies.

Our knowledge of galaxy properties and their evolution through cosmic time has drastically changed from the early 20th century when the Grand Debate (Shapley & Curtis, 1921) between Harlow Shapley and Heber Curtis on the (extra)galactic origin of the so-called nebulae took place (see Trimble (1995) for an interesting discussion on the subject). Since Hubble (1926), Hubble (1929) measurements of these nebulae distances to us, we know they actually are galaxies like our own lying at great distances and moving away from us. This global movement was understood in the cosmological framework of an expanding Universe. In a few months of inter-

val, in 1998-1999, two teams measured the redshift and distance of far distant type Ia supernovae, considered as standard candles, and held evidence for an accelerating expansion which revived the need of a cosmological constant in Einstein's field equations (Riess et al., 1998), (Perlmutter et al., 1999). This additional term has been interpreted as a fluid with negative pressure acting against gravity, and is known as dark energy. Additionally, the first evidence of a dark component in galaxy clusters mass distribution was suggested by Fritz Zwicky (Zwicky, 1933), (Zwicky, 1937). By measuring the relative velocity of 7 galaxies in Coma Berenices, he derived a velocity dispersion σ_v from which he computed with the virial theorem an order of magnitude for the cluster dynamical mass $M_d \sim (\sigma_v^2 R)/G$, with R the cluster characteristic size. The given mass was roughly two orders of magnitude above the expected luminous mass from the luminosity of the galaxies. However, this argument never really convinced the other astronomers at the time. A stronger proof for the existence of a dark component embedded in galaxies came from the study of galaxy rotation curves performed by Vera Rubin (see Fig. 1) in the 1970s (Rubin & Ford, 1970), (Rubin et al., 1978). By looking at the outer material of galaxies, she observed flat rotation curves which either indicated a deviation from Newton's law of gravitation or the presence of large amounts of dark matter in surrounding haloes.

From this point onward, the need of an unified cosmological model including these new aspects became obvious. Decades of observations, state of the art N-body simulations and measurements of cosmological probes have given the actual Λ CDM model its renown. In the

meantime, as cosmology advanced and the size of the Universe exploded following Hubble 1929 publication, a new branch of astronomy centred on galaxies quickly developed both in terms of observations and of theoretical modelling.

1.2 What we have learned about galaxies so far

1.2.1 Evolving properties with redshift ?

Nowadays, galaxies are understood as gravitationally bound collections of stars, gas and dust which are supposed to have collapsed from initial clouds embedded in rapidly growing dark matter haloes. Galaxies formation and evolution should therefore follow the growth of the dark matter distribution through space and time, and as such should be tightly correlated to the global properties of our Universe.

In the local Universe, galaxies can be divided into two categories based on their shape and colour: red ellipticals and blue spirals. These are also referred to as early and late type respectively according to Hubble (1922), Hubble (1926) classification. Even though this is true for most galaxies, we also observe a small fraction of dustier red spirals. Nevertheless, the separation is clear with very few galaxies in between the two populations. Ellipticals tend to be the most massive ($M \sim 1 - 5 \times 10^{11} M_{\odot}$), as well as quenched, that is their Star Formation Rate (SFR) is near 0. Most of their massive younger and bluer stars are gone (as a star's lifetime scales as its mass to the power of -3 or so), leaving only old red stars, which is the reason for their red colour. On the

other hand, spirals are more recent, star-forming galaxies, still full of blue stars, but also smaller and lighter. When looking at more distant parts of the Universe, say $z > 0.5$, this dichotomy is less pronounced. Giant ellipticals are more rare, those found are still forming stars and disk-like galaxies have more irregular morphologies which might be due to past merger events or unrelaxed kinematics because of a recent formation.

In this context, one may wonder how the morphology of galaxies evolved from highly disturbed shapes 10 Gyr ago to the two distinct populations we see today. In order to answer this type of questions, we need to relate the evolution of galaxies morphology to their dynamics. Kinematical observations probe the rotation of gas embedded in galaxies, which can give insights into the processes at play in the formation and settling of gas into discs. It is then possible to

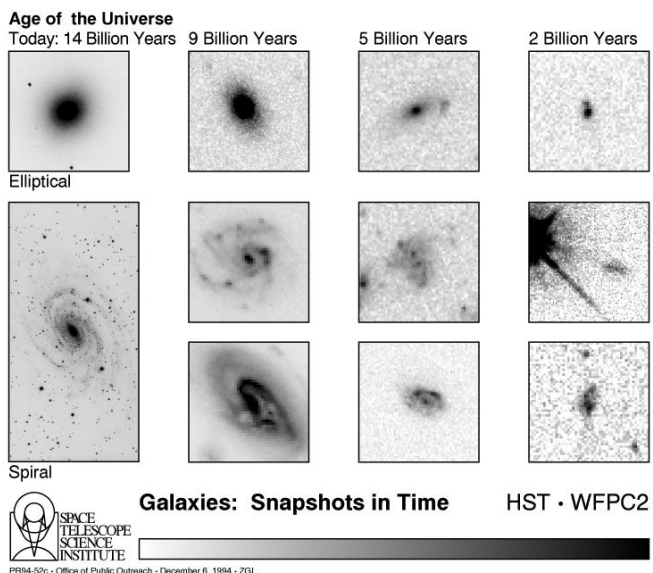


Figure 2: HST images of disk-like and spheroidal galaxies from 12 billion years ago (rightmost column) to the present day (leftmost).

Credits: NASA.

explore the impact of different physical mechanisms such as inflows, outflows, stellar feedback or merging onto these processes. This also gives us access to rotation curves from which we can retrieve information about the dark matter content of galaxies, and explore the angular momentum redistribution through cosmic time. However, in order to study the co-evolution of morphological and dynamical properties with redshift, we need to rely on both morphological (radius, ellipticity) and kinematical parameters such as rotation velocity measurements or velocity dispersions.

Assigning a characteristic rotation velocity and a velocity dispersion to a galaxy is not a straightforward step. Generally, this is done by fitting a model onto some velocity measurement which requires spectroscopic data (3D cube or slit). Almost all galaxies are found to have flat rotation curves because of their dark matter content, though some authors who studied the redshift evolution of stacked rotation curves may have found declining velocity profiles at large radii (Genzel et al., 2017), (Lang et al., 2017). However, this effect might be explained by the choice of the normalisation and does not necessarily imply a smaller fraction of dark matter in high redshift galaxies (Tiley et al., 2019). By flat, we mean that they have a steadily rising slope from the central part until it reaches a turnover point where the curve flattens, a so-called plateau, or where it slowly decreases. In this case, the characteristic velocity which is taken into account is, most of the time, the maximum velocity at the turnover, or the plateau velocity V_{max} . On the other hand, there are various ways of computing the velocity dispersion σ_v , but all ultimately describe the amplitude of unordered, incoherent motion within the galaxy.

In the local Universe, most spirals have low velocity dispersion compared to their rotational velocity. The opposite is true for elliptical galaxies with high velocity dispersion but no significant rotation. For more distant galaxies, this might not be true any more with a much higher fraction of spiral or disk-like galaxies¹ with high velocity dispersion. Usually, the parameter V_{max}/σ_v is used to classify a galaxy as either rotationally supported (> 1) or as dispersion dominated (< 1). High redshift dispersion dominated galaxies were first discovered in the early 21st century (see Glazebrook (2013) for an historical perspective on the subject). These are different from the "dispersion dominated" giant ellipticals we see in the local Universe as they are less massive, more compact and yet highly star forming. Some authors hypothesized that the dispersion dominated galaxies are ancestors of the modern large ellipticals, growing by subsequent merging, or perhaps just the ancestors of the few small ellipticals we see today. Nevertheless, if there is any relation between these two populations, it is still not clear what it is. As we do not know if these dispersion dominated systems are due to unresolved rotation, investigation of the kinematics of new data with better spectral and spatial sampling is mandatory.

¹We will preferentially use the terms disk-like/late-type galaxies rather than spiral as some galaxies studied in the present work do show a disk morphology without clear spiral arm patterns.

1.2.2 An impact from the environment ?

Theoretical modelling based on simple physics principles such as angular momentum conservation, viscous friction, dissipation of energy or gravitational instabilities can account for both the global morphology and kinematics of galaxies. And yet, state of the art N-body simulations including other components such as stellar feedback from supernovae, Active Galactic Nuclei (AGN) with their outflows, and inflows from filaments of gas in the large scale structure of the Universe have shown that these new mechanisms have more impact on the kinematics than previously thought. Moreover, seeing more disturbed morphologies and systems with high velocity dispersion at high redshift seems consistent with the hierarchical growth of dark matter haloes which drive the evolution of galaxies. In this regard, and as haloes will bound galaxies and gas together, we might expect to find a larger fraction of unrelaxed interacting and/or merging galaxies in groups and clusters than for field galaxies, that is those which do not belong to any structure.

Galaxies Star Formation Rate (SFR) will also depend on their redshift and their environment. This is sometimes computed through a scaling law with some gas density (generally neutral hydrogen HI) after accounting for dust attenuation, or by computing a Star Formation History (SFH) through Spectral Energy Distribution fitting techniques (requiring multi-band photometry). As stated above, the star formation is very different nowadays from the past. If we look back in time, we observe an increasing average SFR, reaching a peak around $z \sim 1.5 - 2$ and then decreasing again. This is partially linked to the fact that we observe a larger fraction of spheroidal systems with high SFR than in the local Universe.

Star formation only occurs when there is enough gas supplies to locally gather into collapsing clouds. Once all the gas has been consumed, the SFR is expected to quickly drop to 0 and the galaxy becomes quenched. The question of the impact of the environment on the quenched galaxies we see today is of uttermost importance. Indeed, we expect galaxies found in groups and clusters to lie in hot gas environments which might be fuelled with inflows from filaments of cold gas observed in the large scale structure, or with the galaxies gas content. In the former case, this would imply higher rates of star formation in groups as there is a constant fuelling of gas. On the other hand, if the gas comes from the galaxies through physical processes such as ram pressure stripping, we should see less star forming galaxies in these regions as they might have lost a significant fraction of their content. Isolated field galaxies shall not be stripped of their gas, unless maybe if they are interacting with another galaxy at some point, though such interactions are more rare in these low density regions of the Universe. However, they will also lack inflows of gas, so we might expect to see them quench earlier than their groups and cluster counterparts.

1.2.3 Studying the morpho-kinematical evolution of galaxies

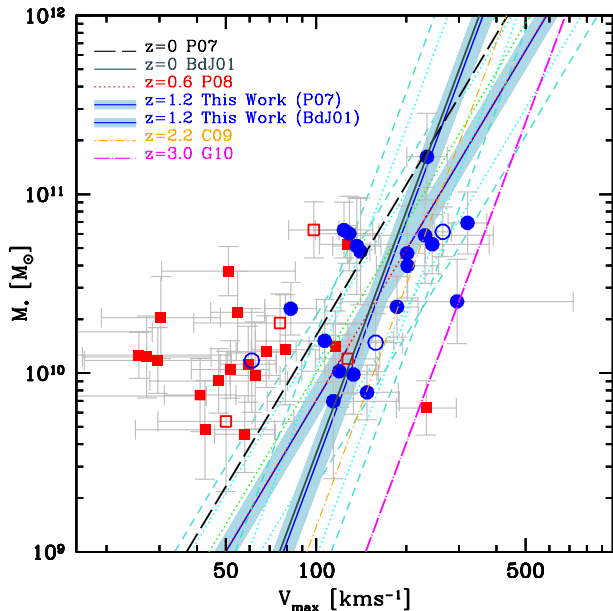


Figure 3: Stellar-mass TFR at $z \sim 1.2$ for galaxies in MASSIV survey from Vergani et al. (2012) (best-fit blue line) compared against two local relations (black, $z = 0$), Puech et al. (2008) (red, $z \approx 0.6$), Cresci et al. (2009) (orange, $z \approx 2.2$) and Gnerucci and Marconi (2011) (magenta, $z \sim 3$). Blue circles represent galaxies classified as rotators ($v/\sigma > 1$) and red squares as non-rotators.

physics is whether or not there is any significant evolution of the stellar-mass TFR with redshift. Some authors, such as in (Puech et al., 2008) and (Vergani et al., 2012), did find an evolution of the TFR zero-point, though others found no significant offset. Thus, there is not clear consensus yet on this subject.

Understanding the evolution of galaxy morphological and kinematical properties through cosmic time is not an easy task. Even though inspecting the velocity field and light profile of a spatially resolved galaxy can be useful to understand the physical mechanisms at work within, we need to perform statistics on large samples if we really want to understand the evolution of the whole galaxy population and not just of a few candidates. One of the most commonly performed morpho-kinematics comparison is the Tully-Fisher Relation (TFR) (Tully & Fisher, 1977), which relates the galaxies masses to their maximum rotational velocity. This is generally compared against the aforementioned V_{\max}/σ_v ratio to distinguish between galaxies with a dominant rotation and those with dominant dispersion.

Rotationally supported galaxies tend to lie on a sequence similar to the local TFR (Pizagno et al., 2007), but dispersion dominated galaxies are actually scattered around this relation (Puech et al., 2008). One of the current hot topics in extra-galactic astro-

1.3 Observation techniques in extra-galactic astronomy

1.3.1 Spectroscopy and photometry

Studying the formation and evolution of galaxies requires large datasets of objects at low and high redshifts. The two types of observation which can be carried out to answer these questions are photometry and spectroscopy. These methods originally yielded different information on the properties of galaxies such as their light distribution, their morphology or their kinematics. Photometry provides 2D images of galaxies whose surface brightness, that is its total flux divided by its solid angle on the sky, is above the surface brightness limit imposed by the instrument limitations, but also whose size is above the instrument resolution. Depending on the band used, we can observe different galactic components, ranging from gas to young/old stellar populations, as well as dust. On the other side, spectroscopy gives us information on the importance of these components with respect to the total emitted light by looking at continuum, emission and absorption lines. Galaxy spectra can contain high continuum values coming from the combination of old and young stellar populations spread through the galaxy. Detected emission lines, such as $H\alpha$, $H\beta$, [OII] and [OIII] doublets or $Ly\alpha$ give us insight into the existence of gas and its ionisation, which can in turn indicate the presence of star-forming zones within the galaxy such as HII regions. Additionally, absorption lines can either show the existence of stars or potentially of intergalactic gas on the line of sight.

From 2D images we can derive morphological parameters such as the ellipticity $e = 1 - b/a$, with b and a the minor and major axes respectively, or some measure of a characteristic radius. Generally, it is assumed that galaxy light profiles have high degrees of symmetry. This implies that a galaxy with an inclination² $i = 0^\circ$ should have circular isophotes (lines of identical surface brightness). When elliptical isophotes are seen, which implies an elliptical shape for the galaxy, this is an indication of a non-zero inclination. Based on our definition, this translates in terms of ellipticity as

$$\cos i = 1 - e \quad (1)$$

This assumption is in fact an approximation given that galaxy discs are not infinitely thin in reality and show more complex morphologies with central bars, spiral arms, satellite galaxies for the largest ones and potential inflows and/or outflows. It is also the case when we study galaxies which have clear disturbed morphologies due to past interactions such as merging events.

In the past, measuring radii and ellipticity were generally done with a curve of growth, consisting in deriving the size and ellipticity of ellipses at different isophote levels. Nowadays, it has become common to fit galaxy light profile models onto images and to recover the morphological parameters from the best fit. One of the most commonly used is a Sérsic profile which is generally

²We define the inclination as the angle between the plane of the galaxy and the plane of the sky, or equivalently between the normal to the plane of the galaxy and the line of sight.

written as (Graham et al., 2005)³

$$I(r) = I_e e^{-b_n \left(\left(\frac{r}{R_e} \right)^{1/n} - 1 \right)} \quad (2)$$

where r is the radial distance to the morphological centre of the galaxy, n is referred as the Sérsic index, R_e is the effective or half-light radius which encloses 50% of the total luminosity, I_e is the intensity at the position R_e and b_n is a term which ensures that R_e does enclose half the total luminosity. By integrating Eq. 2 up to infinity to recover the total luminosity L_{tot} and a second time to R_e so that it equals $L_{\text{tot}}/2$, one can find the definition of b_n to be such that

$$2\gamma(2n, b_n) = \Gamma(2n) \quad (3)$$

with γ and Γ the incomplete and complete gamma functions respectively.

This equation has been widely used in different contexts because of its ability to recover two famous profiles (a) an exponential disc for $n = 1$ which represents a disk-like/spiral galaxy. Here, r is the radial distance in the galactic plane. Sometimes, two exponential discs are used to mimic the vertical variation of the emitted light as well as in the plane of the galaxy. (b) a de Vaucouleurs profile for $n = 4$ which describes early-type galaxies.

Galaxies spectra can have a noisy continuum emission which can make difficult the detection of specific lines. In general, astronomers look at spectral features such as Balmer and Lyman lines, or doublets to improve the confidence in their detection. However, spectroscopes only work in a certain spectral domain, and therefore any line falling out of the instrumental range cannot be detected. When a certain component in a galaxy is observed, this requirement translates in terms of redshift through the equation $\lambda_{\text{obs}} = \lambda_{\text{em}}(1 + z)$. Thus, this implies that galaxies can only be detected in a certain redshift interval.

The measurement of a line can be done through line fitting on a continuum subtracted spectrum. In general, an algorithm finds the redshift of a galaxy by identifying recognisable spectral features and measuring their wavelength offset from their expected rest-frame wavelength. The higher the number of detected lines, the more confidence we have in the redshift. Once this is known, each line is fitted separately with a Gaussian shaped profile from which values of the flux and the dispersion are computed. The shape and dispersion of a line is due to many factors. For galaxies spectra, deviations to Gaussian profiles are not generally considered as these are not spectrally resolved in most cases, except maybe for large mass galaxies (larger velocity gradient). The dispersion is generally affected by the instrumental spectral resolution, beam smearing effects, though not in the case of integrated spectra, the velocity dispersion of the particles on the line of sight, as well as galaxies large scale motion. Beam-smearing effects correspond to a broadening of the intrinsic velocity dispersion because of a combination of the finite instrumental spectral resolution and of the lack of spatial resolution in the central parts of the galaxies.

³The original definition $I(r) \propto e^{-(r/\alpha)^{1/n}}$ from Sérsic (1963) was modified to Eq. 2 because of the immeasurable values α took in practice.

1.3.2 Long slit and early integral field spectroscopy

Before the advent of Integral Field Spectroscopy (IFS), which combines the advantages of both photometry and spectroscopy by providing a spectrum for every pixel in an image, early studies of the rotation curves of galaxies had been done with long slit spectroscopy. In this case, previously known galaxies from photometric surveys were observed with the slit of the spectrograph matching the morphological Position Angle (PA) of the galaxy. This technique therefore assumed that the morphological and kinematical PA are identical, which recent studies might have proven wrong in some cases. The first resolved observation of this kind at high redshift was performed by Vogt et al. (1996) with Keck Telescope. This shed the first light on the resemblance of the rotation curves between galaxies in our local Universe and those found up to $z \sim 1$. Studies of higher redshift galaxies ($2 \lesssim z \lesssim 3$) were first done on star forming UV-selected Lyman Break Galaxies (LBG), whose flux drops in the U-band because of their redshifted Lyman break.

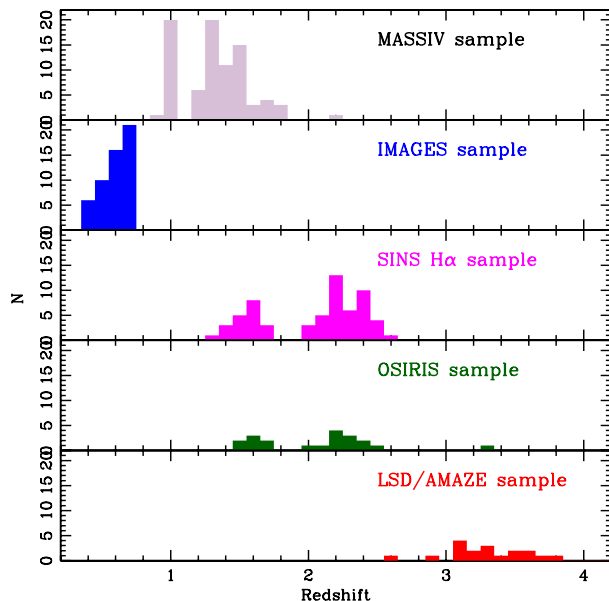


Figure 4: Comparison of the redshift distribution of the main IFS surveys mentioned in the text from Contini et al. (2012).

The very first 3D spectrographs dedicated to the study of galaxies at higher redshift ($z \gtrsim 1$) observed one galaxy at a time because of the lack of a large Field of View (FoV) with good spatial resolution. In that regard, they were used for spectroscopic follow ups of already detected galaxies in photometric surveys. One of these first generation instruments was SINFONI (Eisenhauer et al., 2003) mounted on the Very Large Telescope in Chile, working with both natural seeing and Adaptive Optics (AO). Its corresponding original survey SINS (Förster Schreiber et al., 2009) of 80 objects observed from 2003 to 2008 was one of the first large kinematical IFS survey of its kind. During the following years, others were carried out at intermediate and high redshift. These include the OSIRIS survey (Law et al., 2007) which observed a UV-selected sample of galaxies with OSIRIS IFS on Keck Telescope, the IMAGES survey (Yang et al., 2008) obtained with the VLT's FLAMES-GIRAFFE multi-object integral field facility, as well as the MASSIV survey (Contini et al., 2012) of 84 galaxies with SINFONI in $0.9 < z < 1.8$ (see Fig. 4).

1.3.3 New generation IFS with MUSE

Limitations in terms of FoV, spatial sampling and surface brightness of previous IFS surveys prevented against a thorough study of galaxy kinematics in dense environments, such as clusters, as well as the inspection of low mass and low size galaxies. But with the advent of new generation spectroscopes such as the Multi Unit Spectroscopic Explorer (MUSE) (Bacon et al., 2004) it is

now possible to extend previous analyses to these two unexplored galaxy populations. MUSE is an Integral Field Unit (IFU) mounted on the VLT in Chile, observing in the visible spectrum (wavelength range from 4650 Å to 9300 Å with a resolution $R \sim 3000$). Its wide field-of-view of $1' \times 1'$ and spatial sampling of $0.2 \times 0.2 \text{ arcsec}^2$ combined with its low limiting magnitude (flux detection limit for 10 h of observations is $1.5 \times 10^{-19} \text{ erg s}^{-1} \text{ cm}^{-2}$) allows one to perform blind surveys of galaxies. Its high sensitivity, associated to long exposures, also makes it suitable for the study of low-mass galaxies ($\log_{10}(M/M_{\odot}) < 8.5$, see Contini et al., 2016). Its primary purpose was to study the kinematics of intermediate and high redshift galaxies, and was meant to work both under seeing-limited conditions or with Adaptive Optics. The wavelength range coverage makes it particularly suitable to detect galaxies with high enough [OII] flux in the redshift domain $[0.4, 1.4]$, but any line with high enough Signal to Noise Ratio (SNR) falling in this interval could be detected as well.

2 Sample selection

2.1 MUSE-GTO MAGIC

MAGIC (MUSE-gAlaxy Groups In Cosmos) is an ESO spectroscopic survey (PI: T. Contini) of intermediate redshift ($0.25 < z < 0.85$) groups and clusters performed over 4.5 years (Dec 2014 - May 2019) as part of the MUSE Guaranteed Time Observations (GTO). About 100h of MUSE observing time has been used to cover a sample of 15 groups/clusters selected primarily in the COSMOS area following the group catalogue of (Knobel et al., 2009) and (Knobel et al., 2012). The main objective of this survey is to investigate the impact of environment on the evolution of galaxy properties (SFR, kinematics, metallicity, etc) at intermediate redshifts.

2.2 COSMOS field

Group ID ¹	Ra ² J2000 (°)	Dec ³ J2000 (°)	Exposure ⁴ (hr)	Average seeing ⁵ (")	Total nb. galaxies ⁶	Nb. field galaxies ⁷
CGr32	149.92194	2.520972	3×4.35	0.51 - 0.58	277	113
CGr34_d	149.87766	2.502331	5.25	0.63	74	46
CGr34_bs	149.87766	2.502331	4.75	0.58	74	46
CGr30_d	150.144225	2.065971	9.75	0.67	124	65
CGr30_bs	150.144225	2.065971	6.25	0.57	124	65
CGr84	150.057219	2.599744	5.25	0.59	92	51
CGr84-N	150.05967	2.61275	1	0.51	81	38
CGr114	149.994285	2.258044	2.2	0.68	64	45
CGr79	149.820686	1.821825	4.35	0.60	65	37
CGr28	150.218094	1.812667	1	0.62	49	29
CGr26	150.492767	2.069139	1	0.59	46	31
CGr61	149.728741	1.915987	1	0.64	43	29
CGr51	149.982756	1.801899	1	0.6 – 0.7	44	29
CGr23	149.790782	2.162648	1	0.68	51	32

Table 1: Main characteristics of the MUSE observations in the COSMOS area at the beginning of the internship. Groups ending with _d correspond to deep observations (full stacked OBs) and with _bs correspond to best-seeing observations (only OBs with a seeing below 0.7"). 1. COSMOS group number 2. Group centre's right ascension 3. Group centre's declination 4. Exposure time of MUSE observations 5. Spatial resolution (PSF FWHM) measured in MUSE data and given for the observed [OII] wavelength corresponding to the group's average redshift. 6. Total number of detected galaxies within MUSE FoV 7. Number of field galaxies with a secure redshift $0.4 \leq z \leq 1.4$

The goal of this analysis is to perform a joint study of the morphology and the kinematics of field galaxies at intermediate redshift in the COSMOS area (Scoville et al., 2007) using respectively HST ACS images and MUSE data. To this end, a set of 12 galaxy structures (groups or clusters) was selected. The COSMOS area was chosen because of the large number of multi-band photometric data available for the galaxies in this field and the presence of rich galaxy groups.

Guaranteed Time Observations centred on the groups were performed, from which 14 different MUSE Fields of View (FoV) were obtained. Each is composed of multiple Observation

Blocks (OB) of 40 – 60 min each with the Position Angle (PA) of the instrument rotated by 90° between consecutive exposures. Most of the groups enter into one MUSE FoV, except for CGr32. Since this group⁴ is more extended than the others, three slightly overlapping FoVs were taken around it. A couple of groups were also split into *deep* and *best-seeing* observations, the former combining all the OBs regardless of the average seeing in each OB, when the latter only kept those with an average seeing lower than $0.7''$. The main characteristics of the observed MUSE fields, including the position of their centre, the MUSE exposure time per FoV, the average spatial resolution (PSF FWHM) measured in MUSE data, the total number of galaxies and the number of field galaxies are listed in Table 1.

The structures the MUSE fields were centred upon were chosen from Knobel et al. (2009), Knobel et al. (2012) catalogues. This ensured them to have both a large set of corresponding photometric data available from Laigle et al. (2016) catalogue and HST images with a much better resolution (0.03 arcsec/px for HST). A few galaxies in CGr30_deep might have also been detected within the data cubes but not in HST images. This is because a blind source detection was performed with ORIGIN (Bacon et al., 2017), which can deblend sources even below the PSF, and identify galaxies (mostly at $z > 3$) not seen in broad-band HST images but which are easily detected with MUSE thanks to their bright emission line (mainly $\text{Ly}\alpha$). In addition, there were also a few galaxies detected with MUSE in the vicinity of stars which were masked when creating Laigle et al. (2016) catalogue.

2.3 Prior information on the galaxies

2.3.1 Galaxies in structures

This internship was planned to be similar in many aspects to what V. Abril-Melgarejo, a 2nd year PhD student supervised by B. Epinat at LAM, Marseille, is doing. She studies the morphology and the kinematics of galaxies within the structures observed with MUSE in the same fields as those we are using in this work. The main difference is that we are focusing on "field" galaxies when she only studies those in structures. To differentiate between group and field galaxies, a Friend of Friends algorithm (FoF) was run prior to my arrival on the galaxies in the MUSE fields. Thus, each galaxy was labelled either as belonging to a structure or as "field" galaxies. Additionally, a morphological analysis had already been performed by V. Abril-Melgarejo with GALFIT on galaxies in structures only. Two Sérsic profiles with fixed Sérsic indices ($n = 1, 4$) were used to model the light profile of these galaxies as a combination of a disk and a bulge component. Hence, their intensity can be written as

$$I(r) = I_{e,d} e^{-b_1 \left[\frac{r}{R_d} - 1 \right]} + I_{e,b} e^{-b_4 \left[\left(\frac{r}{R_b} \right)^{1/4} - 1 \right]} \quad (4)$$

where $I_{e,d}$, $I_{e,b}$ are the effective intensities of the disk and the bulge component respectively and R_d , R_b their half-light radii. Therefore, we already have in hand morphological information for roughly half of the total sample including model parameters as described above, but also morphological parameters such as the ellipticity of the galaxies, the position angle of their kine-

⁴which appeared to be a cluster following new redshift measurements using MUSE data.

mathematical main axis (which can be different from the morphological PA), and their size (half-light radius).

2.3.2 Morphological information from COSMOS catalogues

The total number of galaxies detected in the 16 MUSE fields in the COSMOS area is around 1000. Roughly half of them belong to structures and the other half are labelled as "field" galaxies. However, not all of them are useful to our study. Some may be too close to the edge of the MUSE field-of-view, others may be too noisy with a low SNR, or even too small, preventing any relevant kinematical modelling. It is thus mandatory to apply a selection on our data set of field galaxies, first to save time for the analysis, but also to reduce uncertainties.

Our goal is to perform a joint study of the morphology and the kinematics of these galaxies. The tools and the models for the kinematical modelling were already developed as they were used by V. Abril-Melgajero. On the other hand, fitting morphological models with software such as GALFIT (Peng et al., 2002) or SExtractor (Bertin & Arnouts, 1996) would have required additional time which we did not have during this internship. Hopefully for us, morphological modelling had already been performed on some galaxies in the COSMOS field, so we could focus on the kinematical part.

Morphological information can be found in various catalogues and tables⁵. To start with, we decided to use the two most complete we could find, that of Tasca and Cassata. Both catalogues, which are not published but publicly available, contain morphological information including the central position of the galaxy, its half-light radius, concentration and asymmetry parameters, ellipticity, PA of the major morphological axis, and so forth for roughly 232000 galaxies found in the ACS catalogue from Leauthaud et al. (2007). The authors obtained morphological information either with a combination of SExtractor and Morpheus (Abraham et al., 2007), or with GIM2D (Simard, 1998) using HST images.

Since we already had in hand a catalogue combining spectroscopic information (emission line fluxes, redshift, etc.) from MUSE measurements with photometric data from Laigle et al. (2016), we cross-matched it with Cassata's and Tasca's tables to collect their morphological parameters. We cross-matched first with each catalogue separately, and then with both, using the right ascension α and declination δ of the centre of the galaxies, allowing for a maximum separation between the MUSE source and the closest source within the catalogues of 1 arcsec. This procedure was done for structure galaxies as well in order to use them to check the robustness and consistency of the catalogues parameters.

⁵<https://irsa.ipac.caltech.edu/data/COSMOS/tables/morphology/>

2.4 Checking catalogues values consistency

2.4.1 Reasons for checking catalogues values consistency and robustness

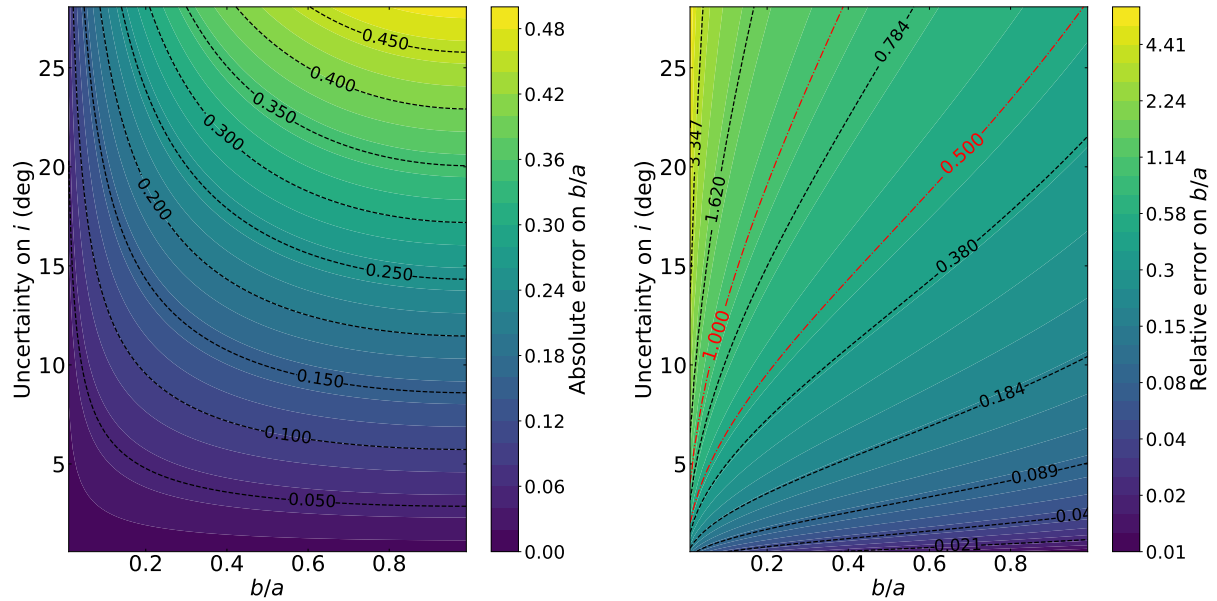


Figure 5: Theoretical uncertainty of the inclination as a function the minor-axis to major-axis ratio b/a and its absolute (left) or relative (right) error. Contours are plotted in black dashed lines, with the red ones corresponding to a 50% and 100% error on b/a . The term error represents here any kind of uncertainty which could be used as an error estimate on b/a . This illustrates the importance to have measures of b/a as reliable as possible for the kinematical modelling.

As a first step, we must select a sample based on relevant criteria. This is meant to ensure that we have reliable morphological and kinematical parameters and to reduce statistical errors. Given that any kinematical modelling relies on prior morphological information (galaxy centre, ellipticity, PA), we can only use a combination of values derived from spectral fitting, for instance the [OII] SNR, and from morphological modelling such as measures of radius and inclination to select our sample.

Before this internship, spectral fitting on the integrated spectra of the galaxies had already been done, and we combined our data with morphological information from COSMOS catalogues as discussed in the previous section. Potentially useful morphological information included half-light radii, magnitudes, ratios of minor to major axis (b/a) or equivalently a measure of the ellipticity of the galaxies. Nevertheless, using this data without checking first how well it compares to values found in other catalogues and/or derived using different softwares/models could lead to high biases. Thus, before discussing any selection criteria for our sample, we must first assess the reliability of the parameters we are going to use in next sections.

Important values to check are the half-light radius, as it will be used to select our sample, the b/a ratio and the PA since these are prior information for the kinematical modelling. We also checked if there was a correlation between the parameters obtained using the bulge/disk decomposition with GALFIT and the catalogues. The axes ratio has a crucial importance since

it is directly related to the inclination of the galaxy on the sky through Eq. 1. Given a certain error $\Delta(b/a)$, and using the variance formula to compute an uncertainty $\Delta f = |\partial_x f| \Delta x$ of a function f , we find for the inclination

$$\Delta i = \Delta(b/a) \left| \frac{b}{a} \left(2 - \frac{b}{a} \right) \right|^{-1/2} \quad (5)$$

This is illustrated in Fig. 5 where Δi has been plotted as a function of b/a and its error (absolute on the left, relative on the right). Contours of the error on b/a have been over-plotted to show how evolves the uncertainty on i given a fixed error on b/a . As expected, the higher the error on b/a the higher the uncertainty on i . An error as high as 50% could yield $\Delta i \approx 27^\circ$, though this value is reached for $b/a \approx 1$ where the axes ratio is the least constrained by the morphology. Nevertheless, Eq. 5 is only a linear approximation and should not be used for too high values of $\Delta(b/a)$. A more appropriate error on b/a of 20% gives a maximum Δi slightly above 10° , which is acceptable. Since the inclination has a strong impact on the galaxy intrinsic maximum rotational velocity, and potentially on the classification of galaxies as rotationally supported or dispersion dominated, this shows we must check carefully that the values of axes ratios are consistent between catalogues.

2.4.2 Catalogues used for comparison

We cross-matched our catalogue of galaxies detected by MUSE in COSMOS with Cassata's and Tasca's. However, as can be seen in Fig. 9 and 10, we found large discrepancies between the parameters. Thus, to better understand their origin, we chose to cross-match our catalogue with another one (Zurich). This table has fewer HST counterparts of MUSE galaxies than in the other two but it contains additional morphological information which we can use for the comparison. In addition to that, we already had GALFIT morphological information on ~ 500 group galaxies with strong confidence in their value. Therefore, we chose to compare the data in the three morphological catalogues with that of GALFIT.

2.4.3 Total magnitudes

The first value we compared is the apparent magnitude. The three catalogues provide a measure of the total magnitude derived from fitting with a single Sérsic profile with a free Sérsic index n on HST images. Given that V. Abril-Melgajero modelled the group galaxies light profiles with GALFIT using two Sérsic profiles with fixed Sérsic indices ($n = 1, 4$), we have two measures of their magnitude: one for the bulge component m_b^{GF} , and another for the disk component m_d^{GF} . To have a meaningful comparison between magnitudes, we need to combine both to get the GALFIT total magnitude. Either component is defined as

$$m_i^{GF} = -2.5 \log_{10} (F_i^{GF}) + C \quad (6)$$

where $i = b, d$ represents either the bulge or the disk, $F = L/4\pi D^2$ is the flux of the galaxy in some band, L its intrinsic luminosity, D its cosmological luminosity distance to us and C a constant which will depend on the band used. Considering that the two components have

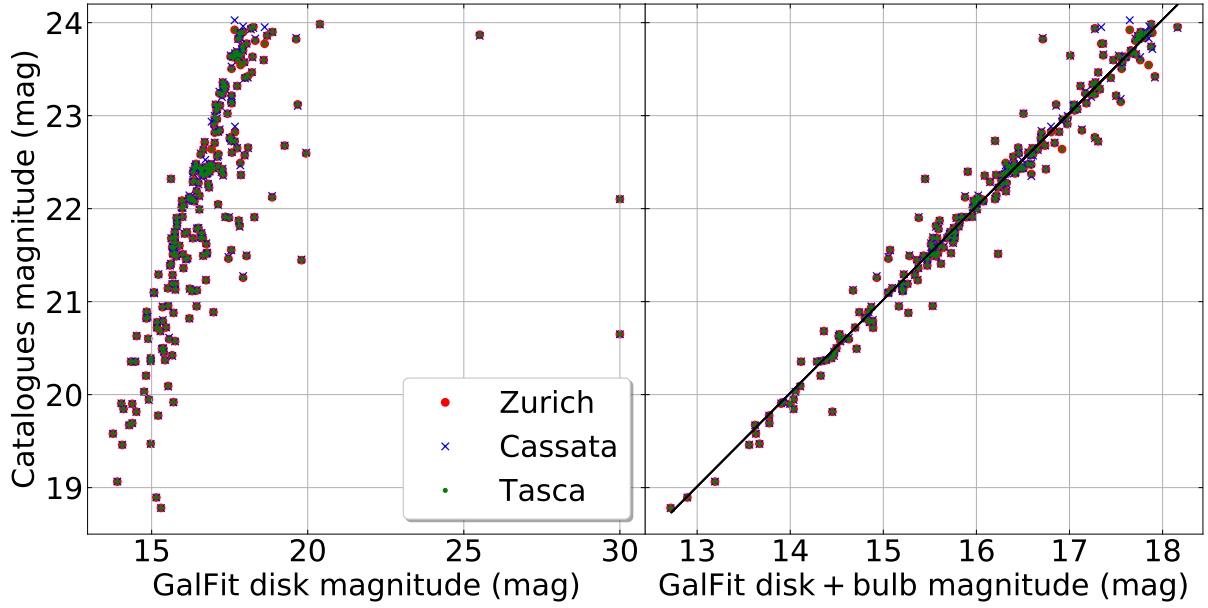


Figure 6: Comparison between the morphological catalogues magnitudes and that of GALFIT for cluster galaxies. Magnitudes from the catalogues agree well between each other. Left: compared with GALFIT disk magnitude only. The slope is too high and a few points are scattered far from the line. Right: compared with the total GALFIT magnitude as defined in Eq. 8. The plain line represents the best-fit linear relation. We find a zero-point offset (5.96 ± 0.04) mag (see Sec. 2.4.3) and a scatter of about 0.2 mag.

different luminosities but are located at the same distance, we can add the fluxes together. Thus the total GALFIT magnitude can also be written as

$$m_{\text{tot}}^{\text{GF}} = -2.5 \log_{10} (F_{\text{b}}^{\text{GF}} + F_{\text{d}}^{\text{GF}}) + C \quad (7)$$

Inverting Eq. 6 to get the components flux as a function of their magnitude and inserting it into Eq. 7 yields

$$m_{\text{tot}}^{\text{GF}} = -2.5 \log_{10} \left[10^{-\frac{m_{\text{b}}}{2.5}} + 10^{-\frac{m_{\text{d}}}{2.5}} \right] \quad (8)$$

This is the value that should be compared with the three catalogues magnitudes. Fig. 6 shows how these scale with each other and with GALFIT disk magnitude on the left, and the total magnitude from Eq. 8 on the right. As expected, the catalogues give the same value except for a few points. We see that the total GALFIT magnitude gives a much better, poorly scattered linear relation with the catalogues magnitudes. Even though there is an offset between GALFIT and the catalogues, this is due to using different conventions for the constant term in Eq. 6.

The same comparison was done on field galaxies, except we did not have GALFIT magnitudes in this case. We also found a good agreement between the catalogues magnitudes.

2.4.4 Morphological type classification

We expect to have some discrepancies in our data because of the models used between GALFIT and SExtractor/GIM2D. To check this effect, we can study how the differences between morphological parameters scale with the morphological type of the galaxies.

For instance, if we use the disk half-light radius of GALFIT to compare with that of SExtractor, we might expect to have some scatter in our relation for the elliptical galaxies as the disk component is not the best one to describe them.

We used the classification given in the three morphological catalogues which are based on different methods. We provide below a short introduction to these classifications:

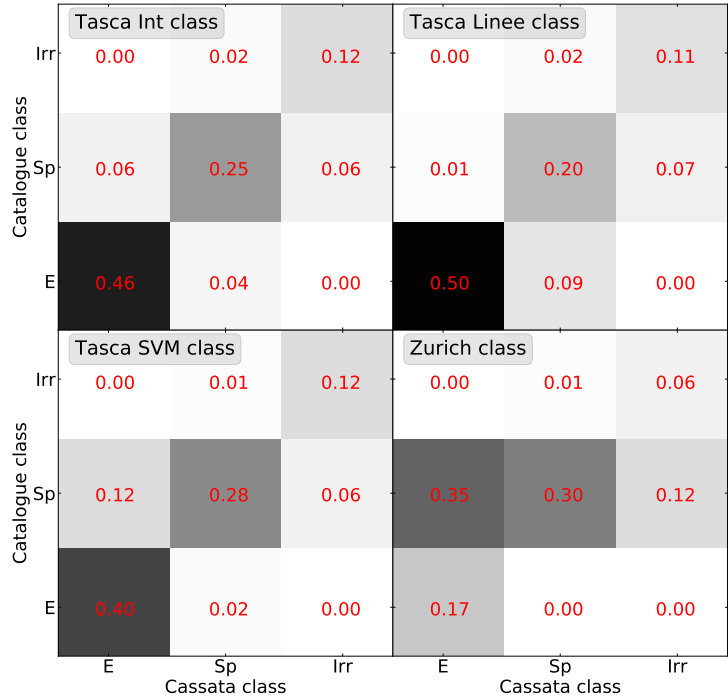


Figure 7: Comparison between morphological types given in Tasca and Zurich catalogues against that of Cassata. Galaxies are labelled as follows: E for ellipticals, Sp for spirals/disks-like, Irr for irregulars. The percentage of galaxies falling into the given classes is indicated in red and the method compared with Cassata's is shown on the top left corner of each plot. We find good agreement between Tasca and Cassata types but not between Cassata and Zurich.

- Cassata's catalogue gives a classification based on their morphological parameters. They use a set of 500 reference galaxies with known parameters which they visually classify either as elliptical, disk-like/spiral or irregular. From this set, each time a new galaxy must be classified, its 11 closest neighbours in parameter space are inspected and the most frequent class among them is assigned to the new galaxy.
- Tasca's catalogue gives different classifications based on three methods. The first is similar to the one used by Cassata. The second one uses the technique described in Abraham et al. (1996) using the asymmetry and concentration parameters. The last one uses a support vector machine to classify the galaxies.
- Zurich's catalogue gives a single classification called Zurich Estimator of Structural Type (ZEST) which is described in Scarlata et al. (2007). This method is based on a Principal Component Analysis (PCA). They only keep the first three Principal Components (PA) which retain most of the information present in the original five parameters (concentration,

asymmetry, Gini coefficient, second-order moment of the brightest pixels producing 20% of the total flux and the ellipticity of the galaxy).

The morphological types given in Tasca’s and Zurich’s catalogues are compared against the class given by Cassata in Fig. 7. We observe a good agreement between Cassata’s and Tasca’s types with just a few elliptical galaxies labelled as disk-like and vice versa. Roughly 50% of the galaxies appear to be elliptical. On the contrary, Zurich’s classification seems to label more than 70% of the galaxies as disk-like, including a large number of elliptical galaxies.

This effect can be better understood by comparing two additional information given in Cassata’s and Zurich’s catalogues. (a) the probability, computed by Cassata, that the given classification is correct. This probability is computed as the number of galaxies within the 11 closest neighbours with the given classification over 11, and it can therefore vary between around 33% and 100%. (b) Zurich’s bulgeness parameter which labels disk galaxies from bulge (0) to disk dominated (3).

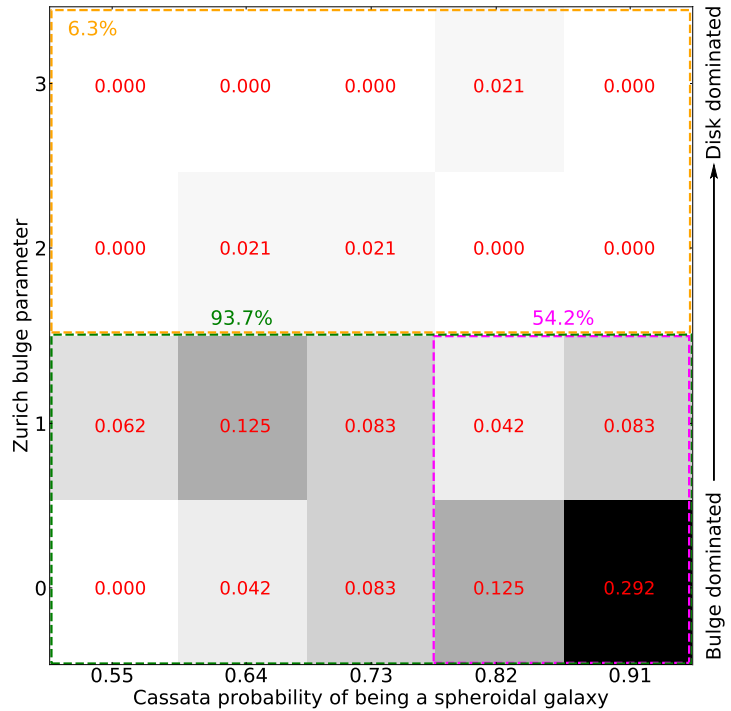


Figure 8: Comparison between Zurich’s bulgeness parameter and Cassata probability that the galaxy belongs to the right classification for spheroidal galaxies (according to Cassata) misclassified as disk-like by Zurich. A low bulgeness value corresponds to a bulge dominated galaxy. We find that more than 93% of galaxies are found to be bulge dominated according to Zurich. Around half of the discrepancy represented in Fig. 7 corresponds to highly probable spheroidal galaxies classified by Zurich as disk-like with a dominant bulge.

This comparison is performed in Fig. 8 for the galaxies classified as spheroidal by Cassata, but as disk-like by Zurich. We find that around half of the discrepancy in the classification comes from galaxies with a high probability of being disk-like in Cassata’s, but with a dominant bulge in Zurich’s. Moreover, if we do not take into account the probability given by Cassata, more than 90% of these galaxies actually have a dominant bulge according to Zurich. Thus, it seems that most of the discrepancy we observe for this population of galaxies in terms of morphological classification is actually due to using different a different vocabulary. Cassata labels them as spheroidal because their light profile is dominated by the bulge component, but Zurich does make the distinction between spheroidal galaxies and disk-like with a dominating bulge.

Considering the aforementioned explanation of the observed discrepancy, and since we find a good agreement between Cassata’s morphological type and those given by Tasca, we decided to use and to stick to Cassata’s class throughout this work whenever we needed to separate galaxies between elliptical/disk-like/irregulars. This choice also ensured us to have the largest sample possible with a coherent classification as Cassata’s catalogue is the one with the largest number of HST counterparts of MUSE galaxies in the COSMOS field.

2.4.5 Half-light radii

Perhaps the most important parameter we have to check is the half-light radius. Indeed, if we underestimate it, we might remove from our sample galaxies which are spatially resolved in MUSE data and therefore reduce our statistics. On the other hand, overestimating it would give us too many unresolved galaxies for which we would spend time removing noise dominated pixels without being able to perform their kinematical analysis in the end. Hence, it is mandatory to thoroughly check the values of the half-light radius from the three catalogues against that of GALFIT, and understand the origin of any discrepancies if there happens to be some.

We found a quite large disagreement between GALFIT half-light radii and those given in the morphological catalogues, as well as between them. This is illustrated in Fig. 9 and 10 where half-light radii in the catalogues are compared against that of GALFIT. Galaxies are colour coded according to the classification given in Cassata’s catalogue. We checked that using Tasca’s classifications as described in Sec. 2.4.4 did not change our conclusions. In these plots, we decided to use for the x-axis the half-light radius of the GALFIT disk component $R_{1/2,d}^{GF}$ for all the galaxies, even though we might expect the ellipticals to be better described by their GALFIT bulge half-light radius. This choice is further discussed below.

The catalogues radii seem to be overestimated with respect to that of GALFIT for low $R_{1/2,d}^{GF}$. Those compared in Fig. 9 and 10 are all derived from SExtractor and, given that it does not take into account the PSF in its fitting routine, we expect the PSF to dominate for galaxies with small angular sizes. On the contrary, GALFIT does take into account the PSF in its calculation, and therefore we expect its half-light radius to decrease with lower values of $R_{1/2,d}^{GF}$. When focussing on galaxies with a GALFIT radius larger than the HST-ACS PSF FWHM which is around 0.15'' (4 – 5 px), we observe a global underestimation for all the catalogues, up to roughly 50%. This scatter is mainly due to elliptical galaxies. On the contrary, radii of disk-like galaxies have the least scatter and bias, especially the values given in Zurich’s catalogue. This different behaviour between elliptical and disk-like galaxies might be explained, as mentioned above, by the fact that we are using the half-light radius of GALFIT disk component to assess the reliability of the elliptical galaxies radii given in the catalogues. A better choice may be to use the bulge component, which better describes the light profile of an elliptical galaxy, and its half-light radius for this population.

If we split the galaxies into two categories, ellipticals and disks/irregulars, and if we use for the first category the bulge radius $R_{1/2,b}^{GF}$, and for the second $R_{1/2,d}^{GF}$, we find that elliptical galaxies half-light radii from the catalogues are now underestimated with GALFIT as shown in Fig. 9 lower plot. These results suggest that elliptical galaxies in this sample are neither dominated (in terms of radius) by the disk component, nor by the bulge in the GALFIT model. Even though we did not push further the analysis on this discrepancy, we still mention that the next step should be to directly compute the half-light radius of the GALFIT model by integrating Eq. 4 up to half its total luminosity.

Based on Fig. 10, we decided to use the galaxies half-light radii given in Zurich catalogue,

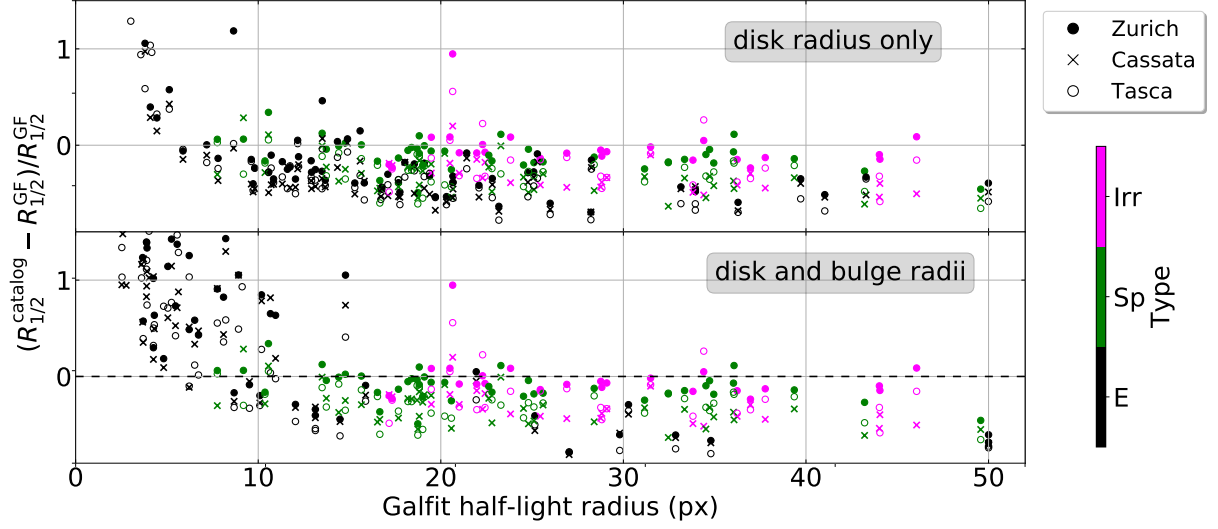


Figure 9: Relative error on the half-light radius between the catalogues and GALFIT. Points have been colour coded according to their classification given in Cassata’s catalogue (Irr for irregular, Sp for disk-like, E for spheroidal). Top: GALFIT disk radius is used for all the points. We observe an underestimation of the catalogues radius with respect to that of GALFIT for elliptical galaxies. Bottom: same plot with GALFIT bulge radius used for elliptical galaxies. In this case, we find an overestimation of the radius.

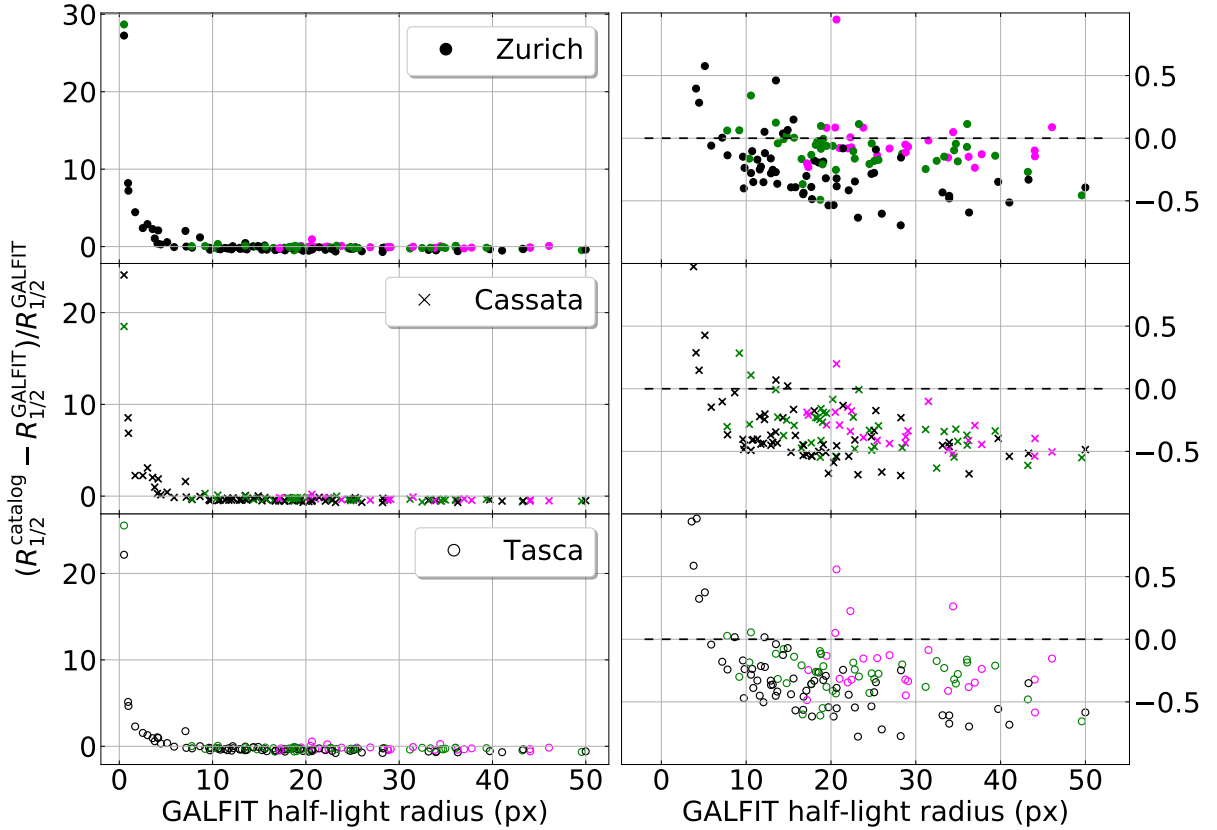


Figure 10: Comparison between half-light radii from the morphological catalogues and the radius of GALFIT disk component. This plot is similar to Fig.9 top plot but each catalogue was separated in its own subplot. Left: full range of relative error. Right: a zoom on the points with $R_{1/2}^{\text{GF}} \geq 5$ px.

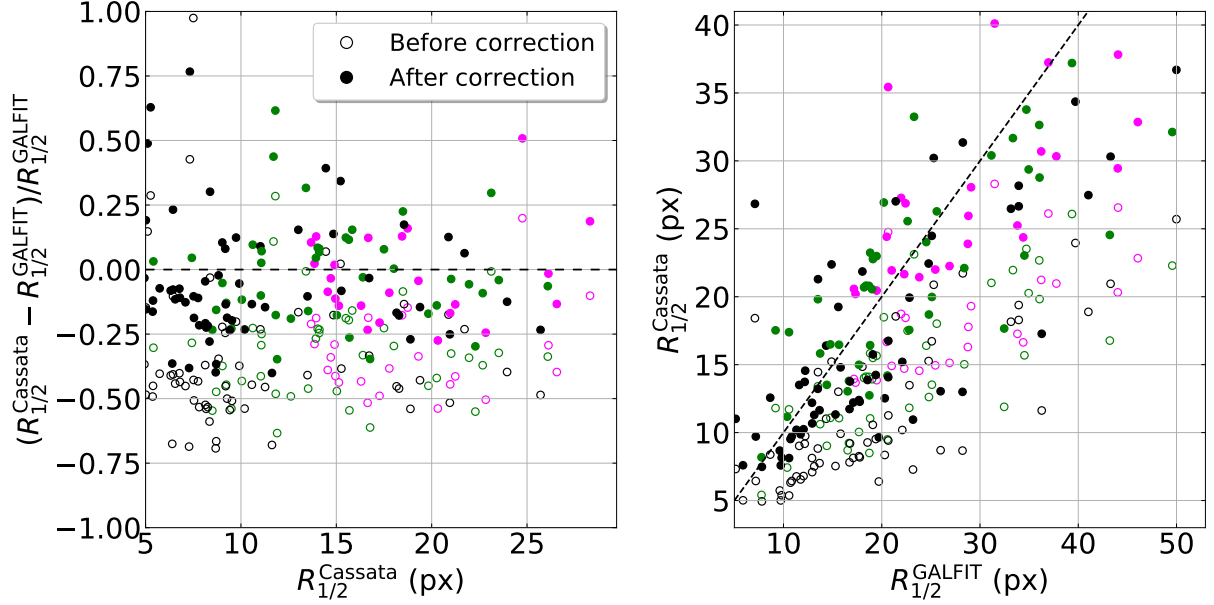


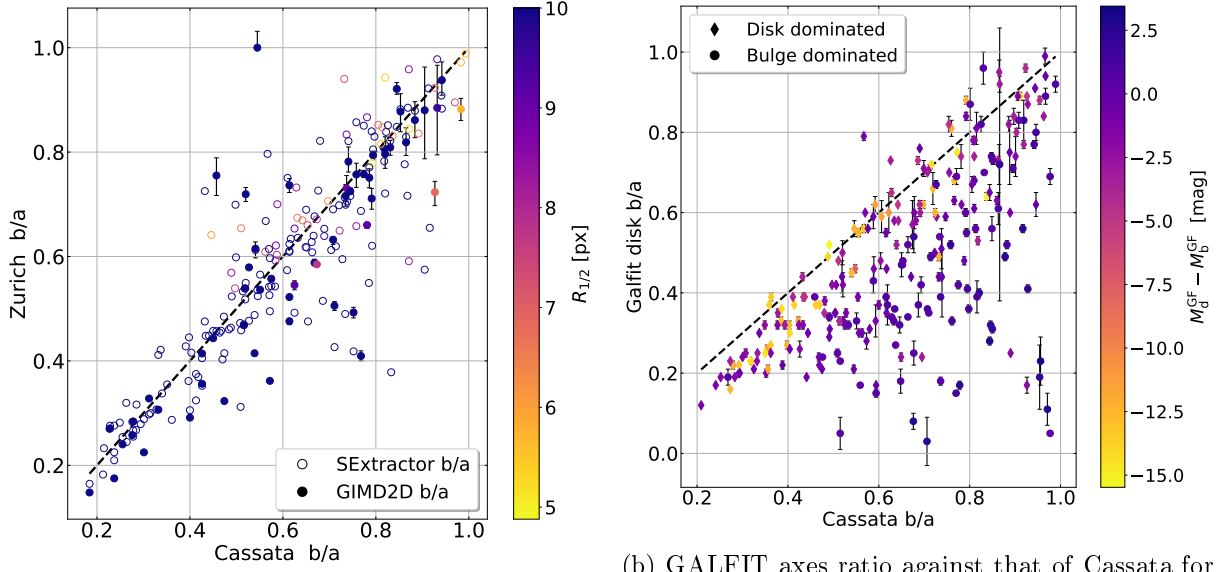
Figure 11: Bias and scatter before and after applying the correction mentioned in the paragraph. The dashed line represents the 1-1 line if there was no bias. Left: half-light radius relative error as a function of Cassata’s radius. Right: scaling between Cassata’s and GALFIT radii. The scatter around 0.2px is not significantly changed after the bias correction.

keeping in mind that we might have a non-negligible fraction of elliptical galaxies for which their value may be underestimated. However, this is the catalogue with least HST counterparts. Thus, in order to increase our sample, we also chose to select additional galaxies found in Cassata’s catalogue but not in Zurich’s. As it seems that Cassata’s radius is more bias than Zurich’s, we fitted a linear relation onto the relative error data, which translates as

$$R_{1/2}^{\text{Corrected}} = R_{1/2}^{\text{Cassata}} \left(1 + \beta + \alpha R_{1/2}^{\text{Cassata}} \right)^{-1} \quad (9)$$

where $R_{1/2}^{\text{Corrected}}$ is the new half-light radius after the bias correction and α, β the parameters of our fit. Based on previous arguments, we only fitted galaxies for which $R_{1/2}^{\text{GF}} > 5$ px. Once a best fit solution was found, we slightly adjusted it by applying a weight on ellipticals in order to limit their impact on disk-like galaxies radii which appeared to be too much overestimated without. We find $\alpha = 1.95 \times 10^{-3}$ and $\beta = -0.349$, which gives us 261 field galaxies. We kept Zurich radius whenever a galaxy had one, and the bias corrected Cassata radius when we only had this value.

2.4.6 Ellipticity



(a) Axes ratio from Zurich and Cassata for the field galaxies. There is an overall good agreement between the catalogues and between Zurich and GIM2D. We find a similar dispersion for SExtractor and GIM2D of about 0.1. No specific trend is found with the galaxies size.

(b) GALFIT axes ratio against that of Cassata for galaxies in structures. Globally, the axes ratio in the catalogue seems to be underestimated. If we separate the galaxies as disk or bulge dominated according to the most luminous component, we find that most of the scatter comes from elliptical galaxies.

Figure 12: Comparison between Cassata, Zurich and GALFIT b/a axes ratio. Zurich catalogue gives two values computed with SExtractor and GIM2D, and Cassata only with SExtractor. Error bars are only available for a few GIM2D and GALFIT values.

As mentioned in previous sections, the ellipticity is a critical parameter which is used to compute a value for the inclination of the galaxies. It is related to the b/a ratio given in the catalogues, so we can compare it as a proxy for the ellipticity. This is illustrated in Fig. 12 (a) where the axes ratio is compared for field galaxies for which we could assign a radius as described in Section 2.4.5. In Fig. 12 (b) where GALFIT b/a is compared with that of Cassata for galaxies in structures. Catalogues give consistent values for field galaxies with most of the scatter coming from the region where $0.4 < b/a < 0.8$. We checked that the size of the galaxies did not impact too much on the error, but we did not find any specific trend. We also checked that catalogues values are comparable to that of GALFIT. In this case, we find a large scatter with the catalogues axes ratio underestimated with respect to GALFIT value for almost all galaxies. Since GALFIT fits two components on the light profile, we expect the galaxies with a dominant bulge to have a less constrained b/a ratio. To check this effect, we colour coded the points according to the difference in magnitude between GALFIT disk and bulge components $M_d^{\text{GF}} - M_b^{\text{GF}}$. We observe that the majority of the scatter actually comes from bulge dominated galaxies, i.e. ellipticals, for which $M_d^{\text{GF}} - M_b^{\text{GF}} > 0$.

2.5 SNR and size selection

2.5.1 Size selection

The first parameter we can think of to make our selection is the size of the galaxies. We already checked in Section 2.4.5 biases which might arise, investigated their origins, and corrected them. Now that we have reliable values, we need to define a selection criterion. Based on Bacon et al. (2015) and Bacon et al. (2017), the MUSE Point Spread Function (PSF), that is the pattern we obtain when we observe a point-like source with MUSE, can either be described by a Moffat (1969) or a Gaussian profile. In practice, they showed that a Gaussian best fits the PSF for MUSE images, so we used this profile in the following parts whenever we needed an estimate of the PSF.

The PSF Full Width at Half Maximum (FWHM) is directly related to the seeing conditions, and it can be easily derived from the relation $I_{\text{PSF}}(\text{FWHM}/2) = I_0/2$. Since it gives us information about the minimum spatial extent within which we start to lose information, we could use it as a starting point for our selection criterion. Moreover, we will need a reliable measure of the PSF FWHM for each galaxy when performing the kinematical modelling. Indeed, according to the aforementioned articles the value of the FWHM is expected to linearly decrease with wavelength. All galaxies are observed via their [OII] $\lambda\lambda 3729, 3729 \text{ \AA}$ doublet at the same rest-frame wavelength. But, given that they are all located at a different redshift z , we actually observe them at wavelengths covering the entire MUSE spectrum, that is we have the usual relation $\lambda_{\text{obs}} = \lambda_{\text{em}}(1+z)$, where λ_{em} , λ_{obs} are the emitted (rest-frame) and observed wavelengths respectively. Therefore, there is not just one FWHM value per field, but one per galaxy.

To derive this value, we need to compute the linear evolution in each field by measuring the FWHM of stars for at least two different wavelengths. Assuming seeing conditions are similar within a field (no spatial dependence), we can use the same relation per MUSE field to compute the FWHM for the observed [OII] wavelength at the redshift of the galaxies. These measures had already been done by B. Epinat and V. Abril-Melgajero on at least two stars per field. Though a more rigorous modelling of the wavelength variation of the PSF FWHM including both more data points and potentially higher order terms is mandatory for future analysis, we decided to stick to these values in the present work, keeping in mind the uncertainties which will affect the velocity dispersion maps in the modelling section. A representation of the FWHM variation with wavelength for the 16 MUSE fields is shown in Fig. 23. Most MUSE fields have FWHM values below $0.7''$ which is not surprising given that it was one of the constraints of the observations.

To have a criterion which is not galaxy dependent, we decided to keep galaxies with a size $2R_{1/2} \geq 0.7''$ since this corresponds to an upper limit for the FWHM for almost every field. Moreover, according to Swinbank et al. (2017) who compared the half-light radius of the nebular [OII] emission in MUSE images with that of their HST counterpart in ACS *I* or WFC3 *H*-band, the [OII] half-light radius seems to scale with the broad-band continuum HST radius as

$$R_{1/2}^{\text{OII}} = (1.18 \pm 0.03) R_{1/2}^{\text{HST}} \quad (10)$$

Thus, by using an upper limit, we may loose a few galaxies which might have been resolved enough. Nevertheless, given the time constraints, this was mandatory if we wanted to keep a sample of reasonable size.

2.5.2 SNR selection

The other information we use to select our sample is the signal to noise ratio. The SNR is generally derived as the ratio between the source's signal and the background level. The noisier an image, the lower the SNR is. Given that galaxy pixels dominated by noise will be removed before the modelling by an automatic cleaning routine, we would like to keep galaxies with a high enough SNR, so that there is still a significant amount of pixels useful for the analysis after the cleaning. In the MUSE pipeline, PLATEFIT (Tremonti et al., 2004) was run on the integrated spectrum of the galaxies after deriving their redshift. This software uses a set of stellar spectra from Bruzual and Charlot (2003) and Sánchez-Blázquez et al. (2006) to fit and remove the continuum emission at the galaxy redshift. Each line is then fitted by a Gaussian profile individually with the same velocity offset and dispersion for all the lines. PLATEFIT returns galaxies spectral parameters such as the [OII] flux. From these, we used the flux and its error to compute a value for the SNR

$$\text{SNR} = \frac{[\text{OII}] \text{ flux}}{[\text{OII}] \text{ flux error}} \quad (11)$$

Since the typical SNR value used by the routine to remove noise dominated pixels in the MUSE maps is around 5, we decided as a first step to choose an SNR lower limit of 10 on the [OII] flux measured in integrated spectra, allowing us to keep galaxies with strong enough detection.

2.5.3 Inspecting galaxies

We visually inspected galaxies around the SNR and the size cuts in order to quantify (a) how many resolved galaxies would be lost if we applied the criteria given in Sec. 2.5.1 and 2.5.2 (false negative) (b) how many unresolved galaxies would be selected in our sample (false positive). To do so, we defined four boxes: $5 \leq \text{SNR} \leq 10$, $10 \leq \text{SNR} \leq 15$, $0.25'' \leq R_{1/2} \leq 0.35''$ and $0.35'' \leq R_{1/2} \leq 0.45''$ containing 46, 20, 58 and 49 galaxies respectively. The selected galaxies according to the criteria defined in Sections 2.5.1 and 2.5.2, as well as the the cuts and the boxes are represented in Fig. 13

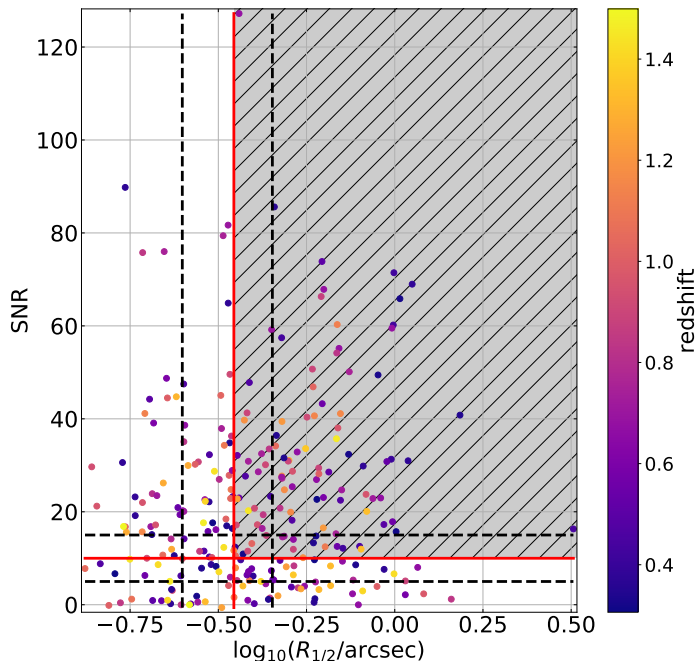


Figure 13: Full sample of 261 field galaxies with our selection box over-plotted (hatched area). Galaxies with $5 \leq \text{SNR} \leq 15$ and $0.25'' \leq R_{1/2} \leq 0.45''$ (bounds plotted as dashed lines) were visually inspected to check how many resolved galaxies we might have lost. Selection criteria from Sec. 2.5 are also plotted as solid red lines. No specific trend appear with redshift.

with $a = 5.866 \times 10^{-8}$, $b = -9.187 \times 10^{-4}$, $c = 6.040$. The FWHM and λ (observed wavelength) are in angstroms. Thus, the LSF FWHM will depend upon the redshift of the galaxy as well. It is related to the velocity dispersion via

$$\frac{\sigma_v}{c} = \frac{\sigma}{\lambda_{\text{em}}(1+z)} \quad (13)$$

where $\sigma = \text{FWHM} (2\sqrt{2\log 2})^{-1}$ is the spectral dispersion due to the LSF.

The choice to keep pixels with a velocity dispersion above $\gamma\sigma_v$ was motivated by the fact that sky lines from OH molecules in the atmosphere can generate fake emission lines, mimicking the [OII] doublet. Sky subtraction during the data reduction can indeed produce fake residuals

We then ran an automatic cleaning routine for all the decided togalaxies in these boxes. The algorithm used removes any pixel which either has its SNR below 5 or a dispersion below a certain percentage γ of the velocity dispersion σ_v computed from the Line Spread Function (LSF) FWHM. The LSF corresponds to the spectral equivalent of a spatial PSF, and tells us how much the instrument will broaden out an infinitely thin line. According to (Bacon et al., 2017) and (Gu  rou et al., 2017) who measured the LSF variation with wavelength in the Hubble Ultra Deep Field (HUDF) and Hubble Deep Field South (HDFS) and who found that it was stable through time, we computed the LSF FWHM as

$$\text{FWHM} = a\lambda^2 + b\lambda + c \quad (12)$$

with P-cygni profiles for the brightest OH sky lines in the MUSE datacubes. However, these are always found to have a width below the LSF FWHM. So any pixel with a fake detection will be removed with this criterion. The percentage γ , which we chose to be 80%, is meant to not remove pixels with real detection which might have thin lines.

After visually inspecting the galaxy sizes in the cleaned [OII] maps, we classified them as resolved if they had a large enough extension (typically larger than the PSF FWHM) or not otherwise. Among the 261 field galaxies which have morphological information in the catalogues, 103 fall into the limits imposed in Sec. 2.5. We find that roughly 26% of the galaxies below the cuts are actually false negatives and that 15% above them are false positives. Since this classification is purely visual, slightly relaxing the constraints on to whether a galaxy is resolved enough or not allow these values to vary by roughly 10%. Our criteria for the selection therefore seem reasonable, though in future works we might increase our sample by a factor of ~ 1.5 by visually inspecting each galaxy separately.

2.6 Characterisation of the sample

2.6.1 Redshift distribution

The choice of the [OII] $\lambda\lambda 3729, 3729 \text{ \AA}$ doublet for the kinematical analysis was mainly due to the large range of redshift it covers given the MUSE spectral range. We therefore had in our catalogue galaxies spanning a redshift domain from 0.3 to about 1.4. As shown in Fig. 14, we loose after our selection a significant fraction of galaxies at all redshifts, and in particular the majority of the most distant galaxies. It is not surprising to loose galaxies at high redshift as these have the lowest angular sizes on the sky at a fixed physical length. Nevertheless, we are globally selecting more galaxies per redshift bin than we are putting aside. The average and median redshifts are 0.749 and 0.719 for the selected galaxies, 0.809 and 0.750 for the unselected ones. Thus, our sample remains consistent in terms of redshift even after the selection.

2.6.2 Mass-SFR relation

Our sample spans 3 orders of magnitude both in mass and SFR in the ranges $10^{8.07} \leq M/M_{\odot} \leq 10^{11.1}$ and $0.04 \leq \text{SFR}/(M_{\odot} \text{ yr}^{-1}) \leq 126$. We investigate our sample in the mass-SFR diagram in Fig. 15. Star-forming galaxies are expected to lie on a diagonal line $\log M - \log \text{SFR}$ space, with some scatter, called the galaxies Main Sequence (MS). A few highly star-forming galaxies such as starburst galaxies and Ultra Luminous InfraRed Galaxies (ULIRG/LIRG) are generally found above the main sequence. Massive quiescent (low SFR) galaxies can also be found below the MS. In our sample, we recover galaxies on the main-sequence after the selection.

We loose massive galaxies with low SFR which is probably due to the fact that we are selecting galaxies with a high enough [OII] surface brightness. Since [OII] flux comes from ionised regions which correlate with star formation, most quiescent galaxies are eliminated during observation, and the few large enough to be detected will have too low SNR values to be selected. We also loose the very low mass end of our sample ($\log_{10}(M/M_{\odot}) \lesssim 8.5$). This is explained by the fact that there exists a scaling relation between a galaxy mass and its radius so that more massive galaxies are also larger and vice-versa. Thus, it appears that the very low mass end is removed from our sample when performing the size selection.

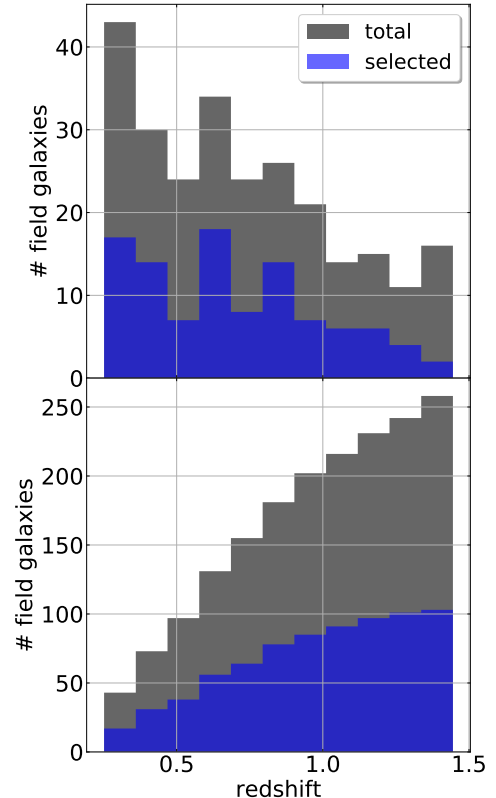


Figure 14: Redshift distribution of the total sample (grey) and selected (blue) galaxies. Redshift bins of size 0.1 have been used. Top: density plot as a function of redshift. Bottom: cumulative distribution. We lack most of the galaxies at redshift 1.4. The redshift distribution of the selected galaxies remains consistent with the original one.

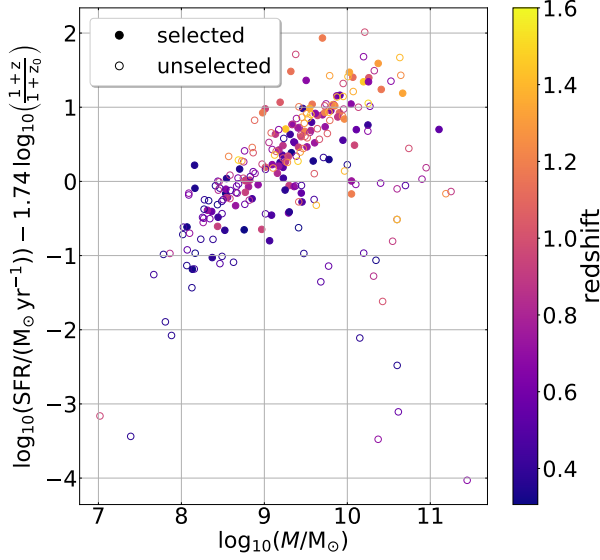


Figure 15: SFR-mass relation for selected (filled circles) and unselected (open circles) galaxies. Left: SFR extracted from SED fitting (Laigle et al., 2016). Right: the redshift corrected SFR as given in Eq. 14. Most of our sample lies on the galaxies main sequence. We are losing almost every massive quiescent galaxies on the lower right part of the plane, as well as the very low mass ones on the lower left.

We also took into account the redshift evolution of the main sequence. We refer to Boogaard et al. (2018) who derived a this evolution for galaxies observed with MUSE in the HUDF on the main-sequence found roughly in the same redshift, mass and SFR intervals. They modelled the log of the SFR as a plane in $\log M - \log(1+z)$ space

$$\begin{aligned} \log_{10} \left(\frac{\text{SFR}}{\text{M}_{\odot} \text{yr}^{-1}} \right) &= 0.83^{+0.07}_{-0.06} \log_{10} \left(\frac{M}{\text{M}_{\odot}} \right) \\ &\quad - 0.83^{+0.05}_{-0.05} \\ &\quad + 1.74^{+0.66}_{-0.68} \log_{10} \left(\frac{1+z}{1+z_0} \right) \end{aligned} \quad (14)$$

where z_0 acts as a normalisation factor which will scale the relation at this redshift. We chose the median redshift of the selected galaxies to apply the SFR correction shown in Fig. 15.

2.6.3 Morphological type

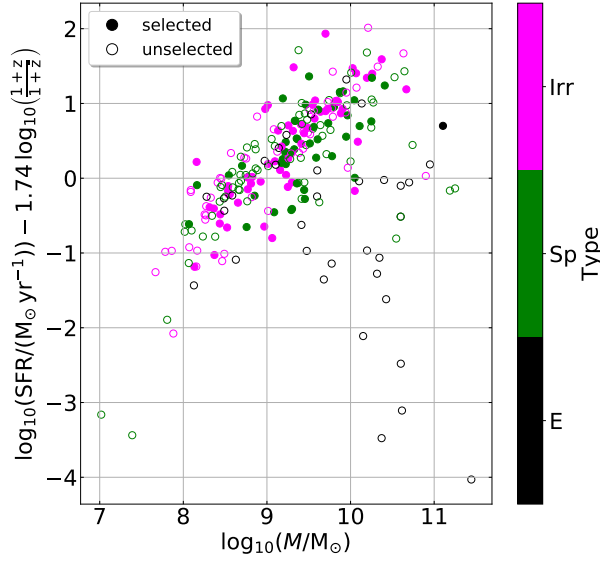


Figure 16: Mass-SFR diagram similar to Fig 15 colour coded according to the galaxies morphological classification. Massive quenched galaxies are all found to be classified as spheroidal systems. After the selection, we only recover irregular and disk-like galaxies, except for one massive star-forming spheroidal galaxy.

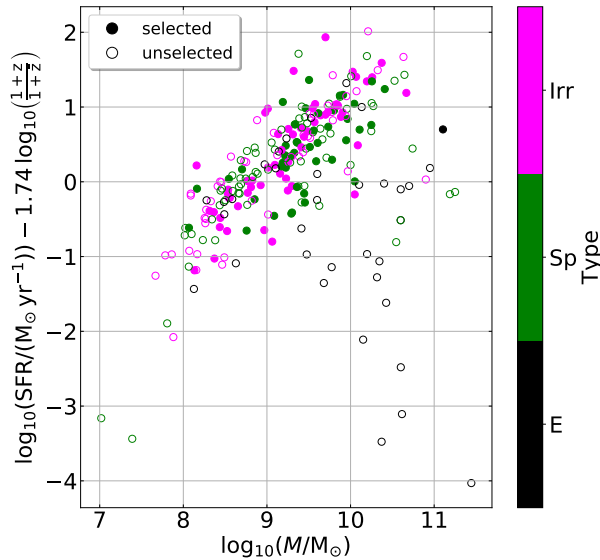


Figure 17: Mass-SFR diagram similar to Fig 15 colour coded according to the galaxies morphological classification. Massive quenched galaxies are all found to be classified as spheroidal systems. After the selection, we only recover irregular and disk-like galaxies, except for one massive star-forming spheroidal galaxy.

To end the characterisation of our sample, we look at which galaxies are selected in terms of morphological type. This is illustrated in Fig.16 where we used Cassata classification to separate galaxies.

We see that the massive quenched galaxies we are not selecting actually are spheroidal systems. Surprisingly enough, we loose every spheroidal galaxy (except one), in particular those found on the main-sequence. In the end, we mainly recover irregularly shaped galaxies and a significant fraction of disk-like galaxies as well.

2.6.4 Inclination of the galaxies

3 Kinematical modelling

3.1 Velocities maps

The velocity field and dispersion maps we used for our modelling, as well as flux and SNR maps, were produced with CAMEL⁶ code. Sub-cubes extracted around the galaxies were first smoothed with a 2D spatial Gaussian (smoothing FWHM below the PSF FWHM to not drastically reduce the spatial resolution) in order to increase the SNR per pixel. A Gaussian profile, and a constant continuum, was then fitted onto every pixel around the [OII] lines. The 3D variance maps produced during the MUSE data reduction were used to weight the contribution of noise induced by sky line residuals. Velocity fields were computed as the average value of the Gaussian in every pixel, and the dispersion maps as the Gaussian dispersion (in velocity space).

3.2 Manual cleaning

For every selected galaxy, we ran the automatic cleaning routine as described in Section 2.5.3. Cleaned maps were produced and the velocity maps were visually inspected. Isolated pixels were removed, even the very few with an identifiable [OII] doublet. We also inspected these lines near the edges and we removed any pixel whose velocity seemed inconsistent with that of its neighbours (typically a velocity offset around $50 - 100 \text{ km s}^{-1}$). Twelve galaxies were found to be spatially unresolved with MUSE despite being selected, and 3 were too close to the edges of the MUSE fields which resulted in missing data. Relaxing the SNR threshold in the routine to 3 allowed us to recover 6 galaxies out of 12.

3.3 Velocity field model

3.3.1 Ramp model

In order to derive the kinematical parameters of our galaxies, we must fit a 2D velocity model onto the cleaned velocity fields. Galaxies kinematical models tend to describe the movement of gas by assuming circular rotation in the plane of the galaxy. The inclination of the galaxy on the sky will have the effect to bend the velocity field and produce a 'spider-diagram' (see Appendix B.1 for more details and Fig. 17 for an example). A few different models exist which might yield slightly different results. Some are derived assuming a certain mass distribution such as Freeman (1970) model of a thin exponential disc. Others rely on a visual description of observed galaxy rotation curves such as the 'ARCTAN' function of Courteau (1997) or the linear ramp model from Wright et al. (2009) and Epinat et al. (2012).

We chose the linear ramp model to describe our velocity fields as it was found to better describe simulated galaxy rotation curves at high redshift

$$V(R) = V_s + V_c \times \begin{cases} R/R_c & \text{if } R < R_c \\ 1 & \text{if } R \geq R_c \end{cases} \quad (15)$$

⁶<https://bitbucket.org/bepinat/camel.git>

This simple model consists in a linearly increasing slope in the central part till it reaches a radius R_c (turnover radius) beyond which the rotation velocity V_c remains the same (plateau). Such a modelling will only work under the assumption of the existence of a measurable global rotation. We also do not take into account features such as a central bar, spiral arms or clumps which are resolved for some galaxies in HST-ACS images. This is because of the lack of spatial resolution in our MUSE data which prevents us from clearly distinguishing these components in the kinematics.

We have in total 3 fixed input parameters which must be known in advance: the inclination, and the centre right ascension and declination. The inclination is used by the model to appropriately bend the velocity field. As discussed in Appendix B.1, there is a degeneracy between the maximum rotation velocity and the inclination of the galaxy so that the kinematical model would not converge to reliable values of i if it were to freely vary. The free parameters are the systematic velocity V_s , the turnover radius and the plateau velocity.

3.4 Beam-smearing and sampling effect on the dispersion

3.4.1 The impact of beam-smearing

The measured velocity dispersion in each pixel is affected both by the real dispersion related to local turbulent motion on the line of sight and by instrumental effects called beam-smearing. If we want to perform statistics on our morpho-kinematics parameters, such as computing a distribution for V_{\max}/σ_v which we can then use to study the Tully-Fisher Relation (TFR) of our sample, we need to derive a physically meaningful value of the average or median velocity dispersion. Our model takes into account this effect when computing a dispersion, but also for the velocity field which will also be impacted by beam-smearing effects. We give, in what follows, a description of the correction applied for the dispersion. This can be easily extended for velocity moments of any order. For more detailed information on the model, we refer to Epinat et al. (2010) from which it is based.

3.4.2 Formalism for the velocity field and dispersion maps

The velocity field is defined as the first moment of the emitting line ([OII] doublet in our case)

$$V(x, y) = \int_{\lambda} L(x, y, \lambda) v(\lambda) d\lambda / M(x, y) \quad (16)$$

where $L(x, y, \lambda)$ is the line spectral light distribution and $M(x, y) = \int_{\lambda} L d\lambda$ the line flux (zero order moment). On the other hand, the velocity dispersion map is defined as the square root of the (central) second order moment

$$\sigma_v(x, y) = \left(\overline{V^2(x, y)} - \overline{V(x, y)}^2 \right)^{1/2} \quad (17)$$

where $\overline{V^2(x, y)}$ is defined as in Eq. 16 with $v \rightarrow v^2$. However, we have in practice a spectrum with a finite resolution due to spectral sampling. Thus, if we have N contiguous spectral channels $\{\lambda_i\}_{i \leq N}$, and if the line is spectrally resolved, we can rewrite Eq. 16 and 17 with a discrete

summation instead of an integral

$$\overline{V(x, y)} \approx \sum_{i \leq N} S_i(x, y, \lambda_i) v(\lambda_i) / M(x, y) \quad (18)$$

where $S_i(x, y, \lambda_i)$ will be the spectral light distribution in the spectral channel centred on λ_i and $M(x, y) \approx \sum_i S_i$.

3.4.3 Impact of the PSF and LSF

The light distribution in each channel will be convolved first by the LSF and then with the PSF so that $S_i^0 = S_i * \text{LSF} * \text{PSF}$ and $M_0 = M * \text{LSF} * \text{PSF}$. Any raw velocity moment of order α can be computed by substituting $S_i \rightarrow S_i^0$ and $M \rightarrow M_0$ in Eq. 16 with $v \rightarrow v^\alpha$

$$\overline{V_0^\alpha} = [(\overline{V^\alpha} M) * \text{PSF}] / M_0 \quad (19)$$

Given Eq. 19, we can compute the effect of the spatial PSF on the velocity dispersion

$$\begin{aligned} \sigma_0^2 &= \overline{V_0^2} - \overline{V_0}^2 \\ &= \left[\frac{(\sigma^2 + \overline{V}^2) M}{M_0} \right] * \text{PSF} - \left[\left(\frac{\overline{V} M}{M_0} \right) * \text{PSF} \right]^2 \end{aligned} \quad (20)$$

3.4.4 Spatial sampling

The second effect to take into account is spatial sampling. The spectral light distribution is now spatially discretized as follows

$$\begin{aligned} S_1(x_j, y_k, \lambda_i) &= (\Delta x \Delta y)^{-1} \int_{\text{pixel}} S_i^0(x, y, \lambda_i) dx dy \\ &= \langle S_i^0(x, y, \lambda_i) \rangle_{(x_j, y_k)} \end{aligned} \quad (21)$$

so that it corresponds to the average integrated light in a pixel centred on (x_j, y_k) of width Δx and height Δy . By summing Eq. 21 over all pixels, one recovers the total flux as

$$M_1(x_j, y_k) = \langle M(x, y) * \text{PSF} \rangle_{(x_j, y_k)} \quad (22)$$

and more generally any raw velocity moment of order α will be written as

$$\overline{V_1^\alpha}(x_j, y_k) = \left\langle \left[\frac{M \overline{V^\alpha}}{M_1} \right] * \text{PSF} \right\rangle_{(x_j, y_k)} \quad (23)$$

This finally gives us the expression for the measured velocity dispersion affected by beam

smearing effects and spatial sampling

$$\sigma_v^{\text{obs}}(x_j, y_k) = \left[\left\langle \left[\frac{(\sigma_v^2 + \bar{V}^2) M}{M_1} \right] * \text{PSF} \right\rangle_{(x_j, y_k)} - \left\langle \frac{\bar{V} M}{M_1} * \text{PSF} \right\rangle_{(x_j, y_k)}^2 \right]^{1/2} \quad (24)$$

We see in Eq. 24 that we need to know the best-fit velocity field model of our galaxy, as well as the PSF, to invert it and retrieve the real velocity dispersion map $\sigma_v(x, y)$ from the observed one. The main limitation is that we need to know the flux distribution with high resolution, which we do not necessarily have in practice.

3.5 Modelling

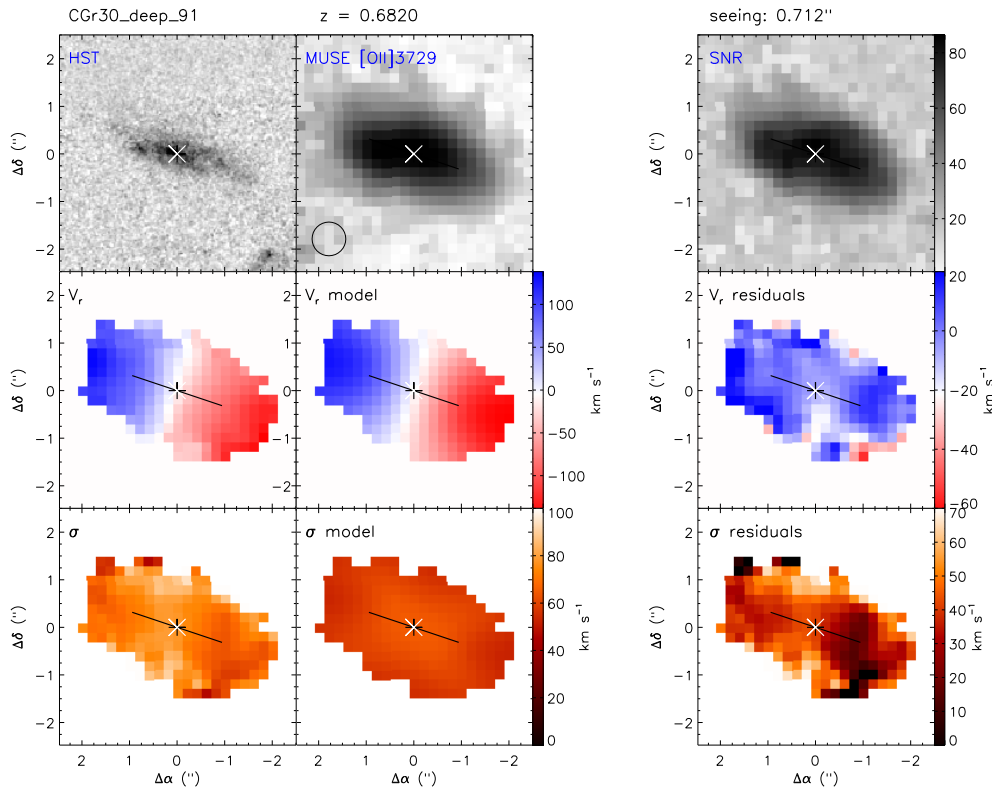


Figure 18: An example of the kinematical model for the galaxy Gr30_deep_91. North is up and East is left. The redshift of the galaxy and the PSF FWHM (seeing) at the observed wavelength are given on top. A circle of radius equal to the FWHM is also represented on top of the MUSE image. From left to right we show Top: HST-ACS image, MUSE [OII] narrow-band image and associated SNR map. Middle: observed [OII] velocity field from MUSE, velocity model and residuals between the two. Bottom: [OII] dispersion map from MUSE, dispersion model of the beam-smearing effect and the residual map corrected of the LSF. The maximum rotational velocity is deduced from the kinematical parameters of the velocity field model. The velocity dispersion is computed from the residual map of the dispersion.

We applied the kinematical model and the beam-smearing correction described in previous sections on the ~ 100 field galaxies of our sample with an IDL routine, from B. Epinat, based on the Markwardt MPFIT IDL library. This code uses a reduced χ^2 method with the

Levenberg-Marquardt algorithm to fit a ramp model on the velocity field, and computes from it the dispersion map after accounting for beam-smearing effects. The derived morphological and kinematical parameters are given in Tables 2, 3 and 4.

We inspected the model against the velocity field for every galaxy, especially the centre position. We expected a couple of MUSE fields to have centre position offsets because of astrometry issues during the data processing. Thus, whenever the centre did seem offset, we moved it in a 3×3 px box and searched for the position with the best χ^2 . The model converged in all cases except for the galaxy **CGr_61_134**. By lack of time, we did not investigate it further and we removed it from the analysis. Our model fits quite well the velocity fields for most of our sample except for 6 galaxies with high χ^2 values, which is due to their disturbed kinematics. An example of a kinematical model is given in Fig. 17 for **Gr30_deep_91**. This is a quite extended galaxy compared to others, at intermediate redshift and with a smooth velocity field. We also flagged 10 galaxies which had poor spatial resolution compared to the remaining sample (generally because of low SNR).

4 Morpho-kinematics analysis

4.1 V_{\max}/σ_v distribution

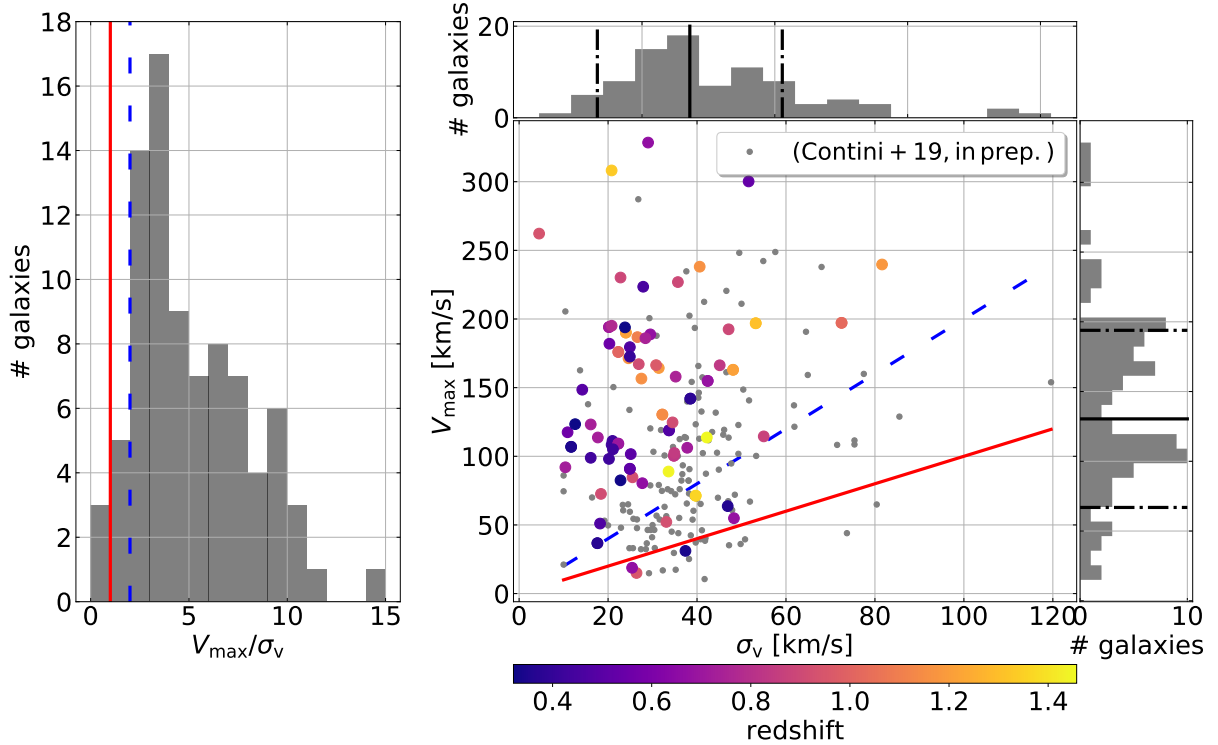


Figure 19: Left: V_{\max}/σ_v distribution. Right: $V_{\max} - \sigma_v$ diagram with galaxies colour coded according to their redshift and the corresponding distributions in terms of maximum rotation velocity and velocity dispersion (median value represented as a plain black line and the dispersion around the median as black dashed dotted lines). The sample of intermediate-redshift galaxies observed with MUSE in the HUDF (Contini et al. 2019, in preparation) is also plotted for comparison. In each plot, two lines, a red plain one for $V_{\max}/\sigma_v = 1$ and a blue dashed one for $V_{\max}/\sigma_v = 2$, are over-plotted to show the separation between dispersion dominated systems (< 1) and rotationally supported galaxies (> 2). We find that 90% of our sample galaxies are rotationally supported.

Intermediate and high redshift galaxies are classified in kinematics studies as either dispersion dominated ($V_{\max}/\sigma_v < 1$) or rotationally supported ($> 1 - 2$). The galaxies velocity dispersion is returned by the model as a parameter, as well as the turnover radius R_c , the plateau velocity V_c and the largest radius where the fit was performed R_{last} . To remain consistent with other studies, we decided to (a) compute the maximum rotation velocity of our galaxies at $R_{\text{max}} = 2.2R_d$, with $R_d \approx 0.5955R_{1/2}$ the disc scale length (see Appendix B.2 for more details). (b) only keep galaxies with a reliable measure of V_{\max} , that is either if $R_{\text{max}} < R_{\text{last}}$ or $R_c < R_{\text{last}}$.

Our sample is represented in Fig. 18 (coloured filled circles) and compared against the sample of intermediate-redshift galaxies observed with MUSE in the Hubble Ultra Deep Field (HUDF, Contini et al. 2019, in preparation). We find that most galaxies (90%) are rotationally supported ($V_{\max}/\sigma_v > 2$). This must be put in contrast with other studies where a higher fraction of dispersion dominated galaxies were found (eg. Förster Schreiber et al., 2009, Law et al., 2009, Gnerucci

& Marconi, 2011, Epinat et al., 2012, Contini et al., 2016). The most probable explanation for such a large fraction is that we use more restrictive selection criteria than in other works. These have removed a substantial fraction of galaxies which are spatially barely resolved with MUSE. However, less restrictive criteria, such as the size threshold in the SNR maps used in Contini et al. (2019), allow one to select small galaxies which are dominated by beam-smearing effects. Therefore, it is not that surprising to find fewer dispersion dominated galaxies in our sample.

We do not find any significant evolution with redshift. Visually, it seems that galaxies with higher dispersion are found at higher redshift. But splitting the sample around $\sigma_v \approx 30-40$ km/s into two categories and computing the median value of the redshift for both populations does not yield a high enough redshift difference given the large dispersion.

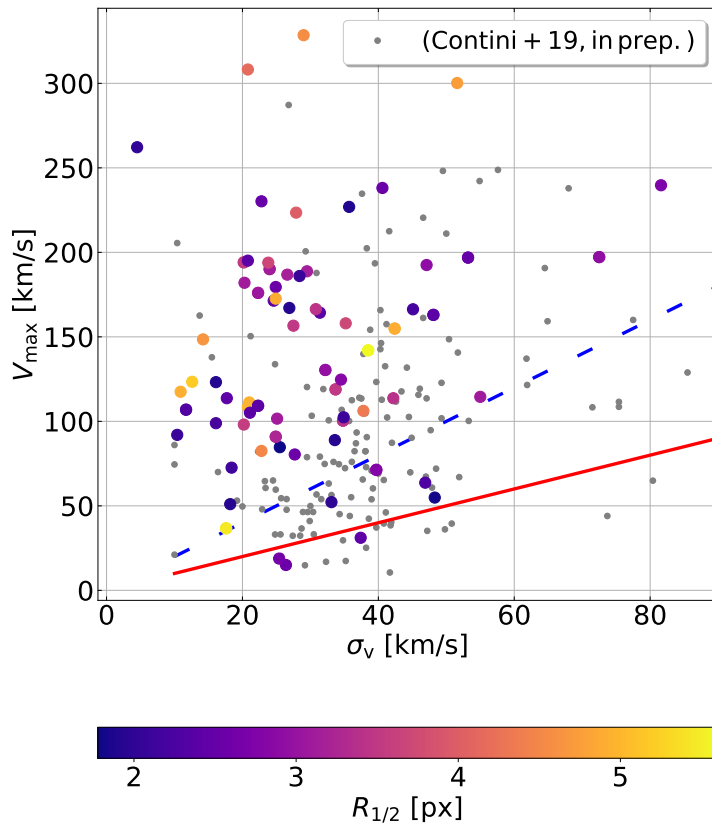


Figure 20: Same graph as in Fig. 18 right plot where the galaxies have been colour coded according to their apparent size on the sky. The dispersion dominated galaxies all have small sizes, but at larger radii we do not find a clear link between size and V_{\max} or σ_v .

We checked the effect of size selection on the V_{\max}/σ_v distribution as shown in Fig. 19. We do not find a clear relation between the half-light radius and the rotation maximum velocity, nor the velocity dispersion. But, we do observe that all the dispersion dominated galaxies, as well as those classified as in between ($1 < V_{\max}/\sigma_v < 2$) are all found to be among the smallest ones. Nevertheless, with less than 10 dispersion dominated objects, it is difficult to conclude. In principle, one should perform the kinematical modelling for the unresolved, beam-smearing dominated galaxies and compare the V_{\max}/σ_v distribution of this population with ours to see how the size selection criterion would translate in terms of the proportion of dispersion dominated systems.

It is possible to relate the ratio between the maximum rotation velocity and the velocity dispersion to the gas fraction in galaxies. Toomre (Toomre, 1964) provided an estimate of the gravitational stability of rotating gas parcels and showed that the rotation of disks ($f_c \approx \Omega^2 R$) cannot counter-balance their gravity ($f_g \approx \pi G \Sigma$) if their length is below $L_{\text{crit}} = (\pi G \Sigma) / \Omega^2$. This can be compared with Jean's instability which occurs when $L > L_J \approx \sigma_v^2 / (G \Sigma)$. The

combination of the effects of gravitational and centrifugal accelerations are summarised in the Toomre parameter

$$Q = \frac{\kappa \sigma_v}{\pi G \Sigma_{\text{gas}}} \approx \frac{\sigma_v}{f_{\text{gas}} V_{\text{max}}} \quad (25)$$

where $\kappa \approx V_{\text{max}}/R$ is the epicyclic frequency, Σ_{gas} is the gas mass surface density and f_{gas} the fraction of gas in the galaxies. In the case of marginally stable disks ($Q \approx 1$) there should therefore be a correlation between V_{max} and σ_v , though with some scatter as disks will have slightly different gas fractions (see Tacconi et al. (2018); Freundlich et al. (2019)).

4.2 Tully-Fisher Relation

4.2.1 Recovering the TFR

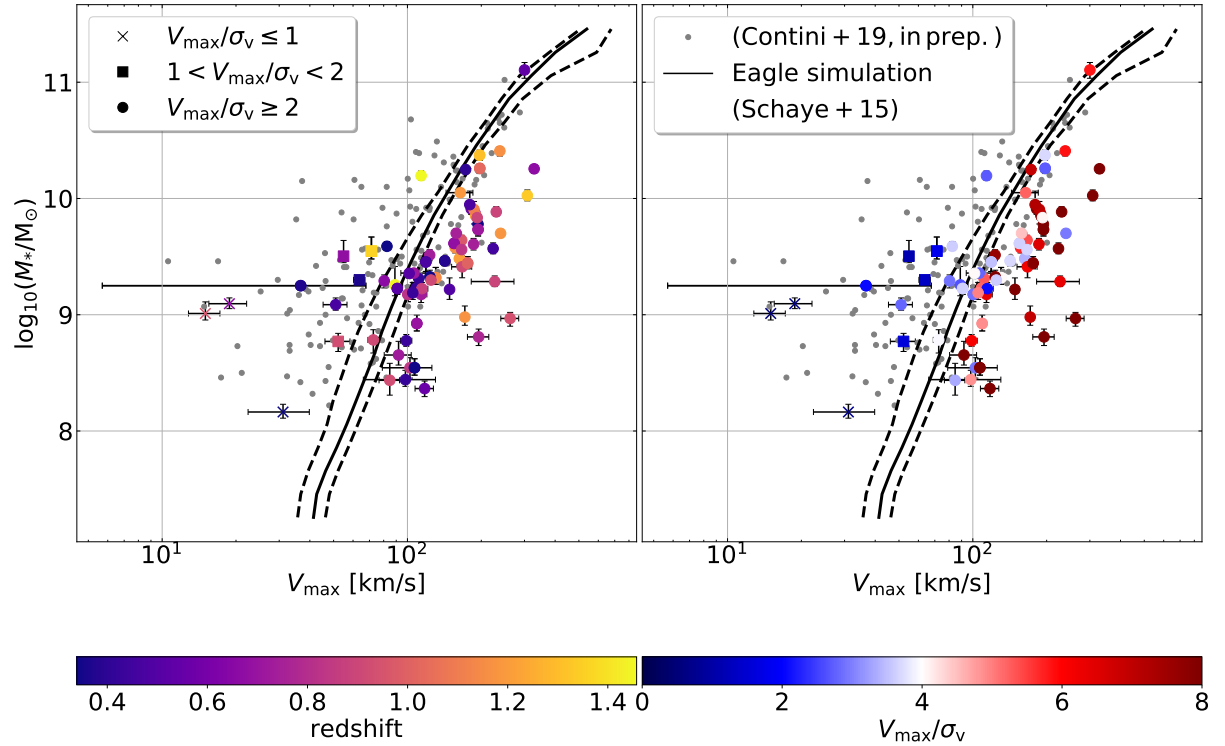


Figure 21: Tully-Fisher Relation Left: as a function of redshift. Right : as a function of V_{max}/σ_v ratio. In both plots, galaxies have been separated between rotationally supported (filled circle), dispersion dominated (cross) and in between (filled square). Error bars correspond to 1σ uncertainties. The TFR from the EAGLE simulation (Schaye et al., 2015) and its errors (plain and dashed lines) are over-plotted for comparison. We also over-plotted (grey points) the results of Contini et al., 2019 (in preparation) for galaxies at similar redshifts observed with MUSE in the HUDF.

We recover the Tully-Fisher Relation (TFR) of our sample galaxies by comparing their stellar masses, obtained with SED fitting and given in Laigle et al. (2016) catalogue, against the maximum (inclination corrected) rotation velocity. In Fig. 20, we compare our TFR with the one derived from the EAGLE suite of hydrodynamical simulations (Schaye et al., 2015) of galaxies in a similar mass range. We also add the results obtained in Contini et al. (2019) discussed in

the previous section.

We find a similar trend between mass and rotation velocity, but globally with an offset towards larger velocities with respect to both the simulations and the MUSE observations in the HUDF. This is consistent with the V_{\max}/σ_v distribution, but also with the lack of dispersion dominated galaxies. Such objects are at the origin of the dispersion in the TFR at lower rotation velocities and lower masses in Contini et al. (2019) sample in Fig. 20. We can also see this effect in our sample where the galaxies with the lowest V_{\max}/σ_v ratio are the most scattered towards lower rotation velocities (see right plot of Fig 20). In terms of redshift, we do not find any evolution of the TFR zeropoint.

4.2.2 A size dependent relation ?

There does not seem to be any obvious correlation between the TFR of our sample and the galaxies redshift or the angular size as can be seen in Fig. 24. However, we do expect to see a correlation between their stellar mass and their size (Mowla et al., 2018). Thus, knowing their angular half-light radius (we will note it $\theta_{1/2}$) and their redshift, we derived their physical size (half-light radius in kpc, we note it $R_{1/2}$ from now on)

$$R_{1/2}(z) = \theta_{1/2} d_A(z) \quad (26)$$

with $d_A(z) = d_c(z)/(1+z)$ the angular diameter distance and d_c the comoving distance. As expected, smaller galaxies have a lower mass and, given the TFR, also have a lower maximum rotation velocity.

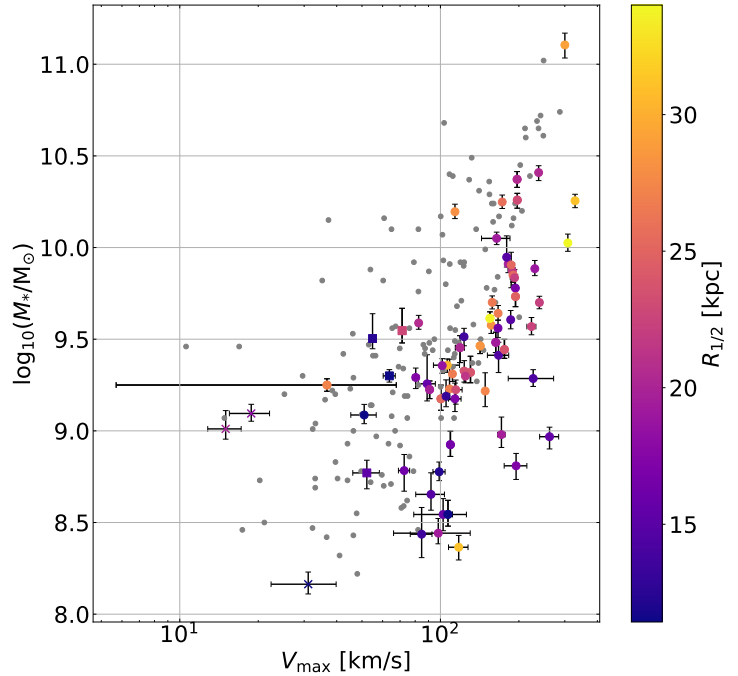


Figure 22: Same plot as Fig 20 (similar legend) but galaxies are colour coded according to their physical size as computed from Eq. 26. We observe a tendency for larger galaxies to be located further up on the TFR (larger masses and rotation maximum velocity).

4.2.3 The effect of inclination

Our TFR in Fig 20 contains the whole sample of spatially resolved galaxies. Even though the maximum rotation velocity is corrected of the inclination through Eq. 29, it still has an impact on the TFR. The kinematics of edge-on galaxies (typically $i \gtrsim 70^\circ$) is less constrained because (a) of the lack of pixels to fit the model. (b) the assumption of an infinitely thin disc on which is based the model is not necessarily met any more. For face-on galaxies ($i \lesssim 30^\circ$), we do generally have plenty of pixels (assuming it is spatially extended enough), but the measured velocity on

the line of sight is also smaller, which requires a better spectral resolution to produce detailed velocity field maps. In addition to that, the relative error on the inclination is greater when it approaches 0° as morphological models can easily converge towards non-zero values of b/a (see left plot of Fig. 5). We therefore checked how the inclination might have impacted our previous TFR. In Fig. 25 we separated our galaxies into two categories: face-on and edge-on galaxies with less constrained kinematics, and those with reasonable values of inclination ($30^\circ \leq i \leq 70^\circ$). Only rotationally supported galaxies with V_{\max}/σ_v are eliminated with this criterion. This is not very surprising since edge-on galaxies need to have a clear disk-like structure to be classified as such, which is generally linked to larger values of rotation velocity. In addition, we expect to have a significant fraction of galaxies with a maximum rotation velocity above the TFR because of the effect of very low inclinations on the sky.

4.3 Scaling between SFR and velocity dispersion

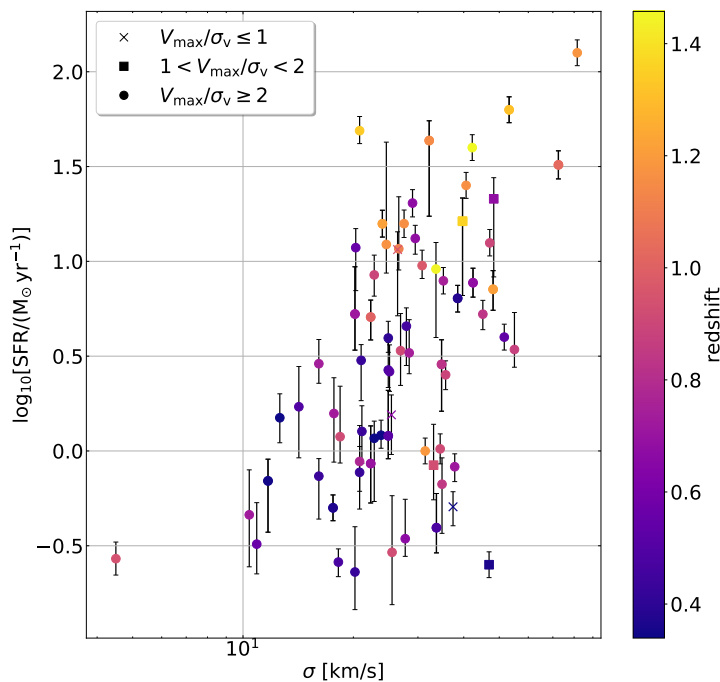


Figure 23: Scaling relation between the star formation rate and the velocity dispersion. We find an evolution as in the SFR – V_{\max} diagram, but with more scatter

dispersion seems to increase with SFR and with redshift, as discussed before, though the scatter is higher than between the SFR and V_{\max} . A similar trend, both in terms of SFR – σ_v relation and redshift evolution on this sequence, was recently found by Hung et al. (2019) in cosmological simulations from the FIRE project (Hopkins et al., 2014). Moreover, if we interpret the velocity dispersion as the effect of energy injection into the gas, it seems consistent to find larger values for higher SFR. This is the conclusion reached by Lehnert et al. (2013) who compared data obtained with SINFONI with simulations of gas rich galaxies, and who found that most of the velocity dispersion was driven by star formation.

Since our galaxies are all located on the main sequence, there exists a relation between the SFR and the mass, with more massive galaxies having higher star formation rates. Given the TFR, we also have a scaling between mass and maximum rotation velocity. Therefore, it seems natural to see a link between the SFR and the rotation velocity in Fig. 26. Interestingly enough, we do observe a redshift evolution. This is mainly due to the redshift evolution of the SFR on the main sequence (see Fig. 15). If we observe such a relation, one may ask if higher a SFR leads to higher velocity dispersion as well. In Fig. 22, we show the variation of the SFR with the velocity dispersion and with redshift. Qualitatively, we can see that the velocity

5 Conclusion and perspectives

The main objective of this five months internship is to perform a morpho-kinematical analysis of intermediate redshift ($0.4 < z < 1.4$) galaxies located in low density environments, with [OII] detection, and observed with MUSE in the COSMOS area. The first part consisted in checking the robustness and consistency of morphological parameters we retrieved from HST catalogues, as well as understanding the origin of any discrepancies. We used two criteria, a bias corrected half-light radius and a SNR threshold, to select a sample of ~ 100 galaxies which are spatially resolved in our MUSE data. After exploring our sample in terms of redshift and mass-SFR, we cleaned the velocities maps of pixels with fake detection. We modelled the galaxies velocity fields assuming a thin rotating disc, and using a ramp model which takes into account beam-smearing effects, the LSF and the inclination. Using the maximum rotation velocity V_{\max} and the velocity dispersion σ_v returned by the model, we provide a first morpho-kinematics analysis of our sample. We find a V_{\max}/σ_v distribution dominated by rotationnaly supported galaxies. We argue that this is most probably due to selection effects and compare it against the results from another survey and a simulation. We also investigate the Tully-Fisher relation, and do not find any evolution with redshift. Finally, we find a correlation between the SFR and the velocity dispersion, and we interpret it as an effect of energy injection into the gas during star-formation.

Only four months have passed since the beginning. Though the main goal has been achieved, the data analysis is not over yet. The next (and last) month of my internship will be dedicated to this task. The different results provided here and their interpretation will be further investigated, especially the TFR and the origin of its offset with respect to other studies. In the short term these results will also be compared against those obtained by V. Abril Melgajero on the group and cluster galaxies observed in the same fields. But this is only possible if we carefully take into account the different selection criteria used. Nevertheless, we should be able to explore the effect of the environment on the morphological and kinematical properties of galaxies at intermediate redshift and on low mass galaxies as well.

In the longer term, that is if this is to be continued into a PhD, there is substantial work to do. In terms of methodology, there is the question of the sample selection. By using less restrictive criteria we could almost double its size, but we need to check in more details how these will affect our conclusions. A larger sample also requires more time for the kinematical modelling. This is also an aspect which could be improved by using more reliable values of the galaxies centres. Another important aspect which has not been covered here is the impact of the kinematical model on our conclusions. Other models exist, some based on mass distributions, which would most certainly yield slightly different values of V_{\max} and σ_v . Therefore, the question is: how much different would they be? In terms of data analysis, we will have only started to answer a few questions about galaxy evolution through cosmic time at the end of the internship. But there are plenty more, from studying the dark matter content of these galaxies (scaling between dynamical and stellar masses across cosmic time?), to investigating the angular momentum redistribution between dark matter haloes and baryons, as well as understanding the impact of merging and gravitational interaction between galaxies on their morphology and kinematics.

References

- Abraham, R. G., Nair, P., et al. (2007, Nov). The Gemini Deep Deep Survey. VIII. When Did Early-Type Galaxies Form? *The Astrophysical Journal*, 669(1), 184-201. doi: 10.1086/521138
- Abraham, R. G., Tanvir, N. R., et al. (1996, Apr). Galaxy morphology to $I=25$ mag in the Hubble Deep Field. *Monthly Notices of the Royal Astronomical Society*, 279(3), L47-L52. doi: 10.1093/mnras/279.3.L47
- Bacon, R., Bauer, S.-M., et al. (2004, Sep). The second-generation VLT instrument MUSE: science drivers and instrument design. In A. F. M. Moorwood & M. Iye (Eds.), *Ground-based instrumentation for astronomy* (Vol. 5492, p. 1145-1149). doi: 10.1117/12.549009
- Bacon, R., Brinchmann, J., et al. (2015, Mar). The MUSE 3D view of the Hubble Deep Field South. *Astronomy and Astrophysics*, 575, A75. doi: 10.1051/0004-6361/201425419
- Bacon, R., Conseil, S., et al. (2017, Nov). The MUSE Hubble Ultra Deep Field Survey. I. Survey description, data reduction, and source detection. *Astronomy and Astrophysics*, 608, A1. doi: 10.1051/0004-6361/201730833
- Bertin, E., & Arnouts, S. (1996, June). SExtractor: Software for source extraction. *Astronomy and Astrophysics Supplement*, 117, 393-404. doi: 10.1051/aas:1996164
- Boogaard, L. A., Brinchmann, J., et al. (2018, November). The MUSE Hubble Ultra Deep Field Survey. XI. Constraining the low-mass end of the stellar mass - star formation rate relation at $z < 1$. *Astronomy and Astrophysics*, 619, A27. doi: 10.1051/0004-6361/201833136
- Bruzual, G., & Charlot, S. (2003, Oct). Stellar population synthesis at the resolution of 2003. *Monthly Notices of the Royal Astronomical Society*, 344(4), 1000-1028. doi: 10.1046/j.1365-8711.2003.06897.x
- Contini, T., Epinat, B., Bouché, N., Brinchmann, J., Boogaard, L. A., Ventou, E., ... Wisotzki, L. (2016, Jun). Deep MUSE observations in the HDFs. Morphokinematics of distant star-forming galaxies down to $10^8 M_{\odot}$. *Astronomy and Astrophysics*, 591, A49. doi: 10.1051/0004-6361/201527866
- Contini, T., Garilli, B., et al. (2012, Mar). MASSIV: Mass Assembly Survey with SINFONI in VVDS. I. Survey description and global properties of the $0.9 < z$ < 1.8 galaxy sample. *Astronomy and Astrophysics*, 539, A91. doi: 10.1051/0004-6361/201117541
- Courteau, S. (1997, Dec). Optical Rotation Curves and Linewidths for Tully-Fisher Applications. *Astronomical Journal*, 114, 2402. doi: 10.1086/118656
- Cresci, G., Hicks, E. K. S., et al. (2009, May). The SINS Survey: Modeling the Dynamics of $z \sim 2$ Galaxies and the High- z Tully-Fisher Relation. *The Astrophysical Journal*, 697(1), 115-132. doi: 10.1088/0004-637X/697/1/115
- Eisenhauer, F., Abuter, R., et al. (2003, Mar). SINFONI - Integral field spectroscopy at 50 milli-arcsecond resolution with the ESO VLT. In M. Iye & A. F. M. Moorwood (Eds.), *Instrument design and performance for optical/infrared ground-based telescopes* (Vol. 4841, p. 1548-1561). doi: 10.1117/12.459468
- Epinat, B., Amram, P., et al. (2008, Aug). GHASP: an $H\alpha$ kinematic survey of spiral and irregular galaxies - VI. New $H\alpha$ data cubes for 108 galaxies. *Monthly Notices of the Royal Astronomical Society*, 388(2), 500-550. doi: 10.1111/j.1365-2966.2008.13422.x
- Epinat, B., Amram, P., et al. (2010, Feb). Evidence for strong dynamical evolution in disc galaxies through the last 11 Gyr. GHASP VIII - a local reference sample of rotating disc galaxies for high-redshift studies. *Monthly Notices of the Royal Astronomical Society*, 401(4), 2113-2147. doi: 10.1111/j.1365-2966.2009.15688.x
- Epinat, B., Tasca, L., et al. (2012, Mar). MASSIV: Mass Assembly Survey with SINFONI in VVDS. II. Kinematics and close environment classification. *Astronomy and Astrophysics*, 539, A92. doi: 10.1051/0004-6361/201117711
- Förster Schreiber, N. M., Genzel, R., et al. (2009, Dec). The SINS Survey: SINFONI Integral Field Spectroscopy of $z \sim 2$ Star-forming Galaxies. *The Astrophysical Journal*, 706(2), 1364-1428. doi: 10.1088/0004-637X/706/2/1364
- Freeman, K. C. (1970, Jun). On the Disks of Spiral and S0 Galaxies. *Astrophysical Journal*, 160, 811. doi: 10.1086/150474
- Freundlich, J., Combes, F., Tacconi, L. J., Genzel, R., Garcia-Burillo, S., Neri, R., ... Salomé, P. (2019, Feb). PHIBSS2: survey design and $z = 0.5 - 0.8$ results. Molecular gas reservoirs during the winding-down of star formation. *Astronomy and Astrophysics*, 622, A105. doi: 10.1051/0004-6361/201732223

- Genzel, R., Schreiber, N. M. F., Übler, H., Lang, P., Naab, T., Bender, R., ... Alexander, T. (2017, Mar). Strongly baryon-dominated disk galaxies at the peak of galaxy formation ten billion years ago. *Nature*, 543(7645), 397-401. doi: 10.1038/nature21685
- Glazebrook, K. (2013, Nov). The Dawes Review 1: Kinematic Studies of Star-Forming Galaxies Across Cosmic Time. *Publications of the Astronomical Society of Australia*, 30, e056. doi: 10.1017/pasa.2013.34
- Gnerucci, A., & Marconi, A. o. (2011, Apr). Dynamical properties of AMAZE and LSD galaxies from gas kinematics and the Tully-Fisher relation at $z \sim 3$. *Astronomy and Astrophysics*, 528, A88. doi: 10.1051/0004-6361/201015465
- Graham, A. W., Driver, S. P., et al. (2005, Oct). Total Galaxy Magnitudes and Effective Radii from Petrosian Magnitudes and Radii. *The Astronomical Journal*, 130(4), 1535-1544. doi: 10.1086/444475
- Guérou, A., Krajnović, D., et al. (2017, Nov). The MUSE Hubble Ultra Deep Field Survey. V. Spatially resolved stellar kinematics of galaxies at redshift $0.2 \lesssim z \lesssim 0.8$. *Astronomy and Astrophysics*, 608, A5. doi: 10.1051/0004-6361/201730905
- Hopkins, P. F., Kereš, D., Oñorbe, J., Faucher-Giguère, C.-A., Quataert, E., Murray, N., & Bullock, J. S. (2014, November). Galaxies on FIRE (Feedback In Realistic Environments): stellar feedback explains cosmologically inefficient star formation. *Monthly Notices of the Royal Astronomical Society*, 445, 581-603. doi: 10.1093/mnras/stu1738
- Hubble, E. P. (1922, Oct). A general study of diffuse galactic nebulae. *Astrophysical Journal*, 56, 162-199. doi: 10.1086/142698
- Hubble, E. P. (1926, Dec). Extragalactic nebulae. *Astrophysical Journal*, 64, 321-369. doi: 10.1086/143018
- Hubble, E. P. (1929, Jan). A Relation between Distance and Radial Velocity among Extra-Galactic Nebulae. *Contributions from the Mount Wilson Observatory*, 3, 23-28.
- Hung, C.-L., Hayward, C. C., Yuan, T., Boylan-Kolchin, M., Faucher-Giguère, C.-A., Hopkins, P. F., ... Wetzel, A. (2019, Feb). What drives the evolution of gas kinematics in star-forming galaxies? *Monthly Notices of the Royal Astronomical Society*, 482(4), 5125-5137. doi: 10.1093/mnras/sty2970
- Knobel, C., Lilly, S. J., et al. (2009, Jun). An Optical Group Catalog to $z = 1$ from the zCOSMOS 10 k Sample. *The Astrophysical Journal*, 697(2), 1842-1860. doi: 10.1088/0004-637X/697/2/1842
- Knobel, C., Lilly, S. J., et al. (2012, Jul). The zCOSMOS 20k Group Catalog. *The Astrophysical Journal*, 753(2), 121. doi: 10.1088/0004-637X/753/2/121
- Laigle, C., McCracken, H. J., et al. (2016, June). THE COSMOS2015 CATALOG: EXPLORING THE $1 < z < 6$ UNIVERSE WITH HALF A MILLION GALAXIES. *The Astrophysical Journal Supplement Series*, 224(2), 24. doi: 10.3847/0067-0049/224/2/24
- Lang, P., Förster Schreiber, N. M., Genzel, R., Wuyts, S., Wisnioski, E., Beifiori, A., ... Burkert, A. (2017, May). Falling Outer Rotation Curves of Star-forming Galaxies at $0.6 \lesssim z \lesssim 2.6$ Probed with KMOS^{3D} and SINS/zC-SINF. *The Astrophysical Journal*, 840(2), 92. doi: 10.3847/1538-4357/aa6d82
- Law, D. R., Steidel, C. C., Erb, D. K., Larkin, J. E., Pettini, M., Shapley, A. E., & Wright, S. A. (2009, Jun). The Kiloparsec-scale Kinematics of High-redshift Star-forming Galaxies. *The Astrophysical Journal*, 697(2), 2057-2082. doi: 10.1088/0004-637X/697/2/2057
- Law, D. R., Steidel, C. C., et al. (2007, Nov). Integral Field Spectroscopy of High-Redshift Star-forming Galaxies with Laser-guided Adaptive Optics: Evidence for Dispersion-dominated Kinematics. *The Astrophysical Journal*, 669(2), 929-946. doi: 10.1086/521786
- Leauthaud, A., Massey, R., et al. (2007, Sep). Weak Gravitational Lensing with COSMOS: Galaxy Selection and Shape Measurements. *The Astrophysical Journal Supplement Series*, 172(1), 219-238. doi: 10.1086/516598
- Lehnert, M. D., Le Tiran, L., Nesvadba, N. P. H., van Driel, W., Boulanger, F., & Di Matteo, P. (2013, Jul). On the self-regulation of intense star-formation in galaxies at $z = 1-3$. *Astronomy and Astrophysics*, 555, A72. doi: 10.1051/0004-6361/201220555
- Moffat, A. F. J. (1969, December). A Theoretical Investigation of Focal Stellar Images in the Photographic Emulsion and Application to Photographic Photometry. *Astronomy and Astrophysics*, 3, 455.
- Mowla, L., van Dokkum, P., Brammer, G., Momcheva, I., van der Wel, A., Whitaker, K., ... Marchesini, D. (2018, August). COSMOS-DASH: The Evolution of the Galaxy Size-Mass Relation Since $z \sim 3$ from new Wide Field WFC3 Imaging Combined with CANDELS/3DHST. *Astrophysical Journal*.
- Peng, C. Y., Ho, L. C., Impey, C. D., et al. (2002, July). Detailed Structural Decomposition of Galaxy Images. *The Astronomical Journal*, 124, 266-293. doi: 10.1086/340952

- Perlmutter, S., Aldering, G., et al. (1999, Jun). Measurements of Ω and Λ from 42 High-Redshift Supernovae. *The Astrophysical Journal*, 517(2), 565-586. doi: 10.1086/307221
- Pizagno, J., Prada, F., et al. (2007, Sep). The Tully-Fisher Relation and its Residuals for a Broadly Selected Sample of Galaxies. *The Astronomical Journal*, 134(3), 945-972. doi: 10.1086/519522
- Puech, M., Flores, H., et al. (2008, Jun). IMAGES. III. The evolution of the near-infrared Tully-Fisher relation over the last 6 Gyr. *Astronomy and Astrophysics*, 484(1), 173-187. doi: 10.1051/0004-6361:20079313
- Riess, A. G., Filippenko, A. V., et al. (1998, Sep). Observational Evidence from Supernovae for an Accelerating Universe and a Cosmological Constant. *The Astrophysical Journal*, 116(3), 1009-1038. doi: 10.1086/300499
- Rubin, V. C., & Ford, J. W. Kent. (1970, Feb). Rotation of the Andromeda Nebula from a Spectroscopic Survey of Emission Regions. *Astrophysical Journal*, 159, 379. doi: 10.1086/150317
- Rubin, V. C., Ford, W. K., Jr., et al. (1978, November). Extended rotation curves of high-luminosity spiral galaxies. IV - Systematic dynamical properties, SA through SC. *Astrophysical Journal*, 225, L107-L111. doi: 10.1086/182804
- Sánchez-Blázquez, P., Peletier, R. F., et al. (2006, Sep). Medium-resolution Isaac Newton Telescope library of empirical spectra. *Monthly Notices of the Royal Astronomical Society*, 371(2), 703-718. doi: 10.1111/j.1365-2966.2006.10699.x
- Scarlata, C., Carollo, C. M., et al. (2007, Sep). COSMOS Morphological Classification with the Zurich Estimator of Structural Types (ZEST) and the Evolution Since $z = 1$ of the Luminosity Function of Early, Disk, and Irregular Galaxies. *The Astrophysical Journal Supplement Series*, 172(1), 406-433. doi: 10.1086/516582
- Schaye, J., Crain, R. A., Bower, R. G., Furlong, M., Schaller, M., Theuns, T., ... Helly, J. C. (2015, Jan). The EAGLE project: simulating the evolution and assembly of galaxies and their environments. *Monthly Notices of the Royal Astronomical Society*, 446(1), 521-554. doi: 10.1093/mnras/stu2058
- Scoville, N., Aussel, H., et al. (2007, Sep). The Cosmic Evolution Survey (COSMOS): Overview. *The Astrophysical Journal Supplement Series*, 172(1), 1-8. doi: 10.1086/516585
- Sérsic, J. L. (1963). Influence of the atmospheric and instrumental dispersion on the brightness distribution in a galaxy. *Boletín de la Asociación Argentina de Astronomía La Plata Argentina*, 6, 41.
- Shapley, H., & Curtis, H. D. (1921, may). The Scale of the Universe. *Bulletin of the National Research Council*, Vol. 2, Part 3, No. 11, p. 171-217, 2, 171-217.
- Simard, L. (1998, Jan). GIM2D: an IRAF package for the Quantitative Morphology Analysis of Distant Galaxies. In R. Albrecht, R. N. Hook, & H. A. Bushouse (Eds.), *Astronomical data analysis software and systems vii* (Vol. 145, p. 108).
- Swinbank, A. M., Harrison, C. M., et al. (2017, May). Angular momentum evolution of galaxies over the past 10 Gyr: a MUSE and KMOS dynamical survey of 400 star-forming galaxies from $z = 0.3$ to 1.7. *Monthly Notices of the Royal Astronomical Society*, 467(3), 3140-3159. doi: 10.1093/mnras/stx201
- Tacconi, L. J., Genzel, R., Saintonge, A., Combes, F., García-Burillo, S., Neri, R., ... Lilly, S. (2018, Feb). PHIBSS: Unified Scaling Relations of Gas Depletion Time and Molecular Gas Fractions. *The Astrophysical Journal*, 853(2), 179. doi: 10.3847/1538-4357/aaa4b4
- Tiley, A. L., Swinbank, A. M., Harrison, C. M., Smail, I., Turner, O. J., Schaller, M., ... Sharples, R. M. (2019, May). The shapes of the rotation curves of star-forming galaxies over the last ≈ 10 Gyr. *Monthly Notices of the Royal Astronomical Society*, 485(1), 934-960. doi: 10.1093/mnras/stz428
- Toomre, A. (1964, May). On the gravitational stability of a disk of stars. *Astrophysical Journal*, 139, 1217-1238. doi: 10.1086/147861
- Tremonti, C. A., Heckman, T. M., et al. (2004, Oct). The Origin of the Mass-Metallicity Relation: Insights from 53,000 Star-forming Galaxies in the Sloan Digital Sky Survey. *The Astrophysical Journal*, 613(2), 898-913. doi: 10.1086/423264
- Trimble, V. (1995, Dec). The 1920 Shapley-Curtis Discussion: Background, Issues, and Aftermath. *Publications of the Astronomical Society of the Pacific*, 107, 1133. doi: 10.1086/133671
- Tully, R. B., & Fisher, J. R. (1977, February). A new method of determining distances to galaxies. *Astronomy and Astrophysics*, 54, 661-673.
- Vergani, D., Epinat, B., et al. (2012, Oct). MASSIV: Mass Assembly Survey with SINFONI in VVDS. IV. Fundamental relations of star-forming galaxies at $1 < z < 1.6$. *Astronomy and Astrophysics*, 546, A118. doi: 10.1051/0004-6361/201118453
- Vogt, N. P., Forbes, D. A., et al. (1996, Jul). Optical Rotation Curves of Distant Field Galaxies: Keck Re-

- sults at Reshifts to Z approximately 1. *Astrophysical Journal Letters*, 465, L15. doi: 10.1086/310136
- Wright, S. A., Larkin, J. E., et al. (2009, Jul). Dynamics of Galactic Disks and Mergers at $z \sim 1.6$: Spatially Resolved Spectroscopy with Keck Laser Guide Star Adaptive Optics. *The Astrophysical Journal*, 699(1), 421-440. doi: 10.1088/0004-637X/699/1/421
- Yang, Y., Flores, H., et al. (2008, Jan). IMAGES. I. Strong evolution of galaxy kinematics since $z = 1$. *Astronomy and Astrophysics*, 477(3), 789-805. doi: 10.1051/0004-6361:20078219
- Zwicky, F. (1933). Die Rotverschiebung von extragalaktischen Nebeln. *Helvetica Physica Acta*, 6, 110-127.
- Zwicky, F. (1937, October). On the Masses of Nebulae and of Clusters of Nebulae. *Astrophysical Journal*, 86, 217. doi: 10.1086/143864

A PSF FWHM variation with wavelength

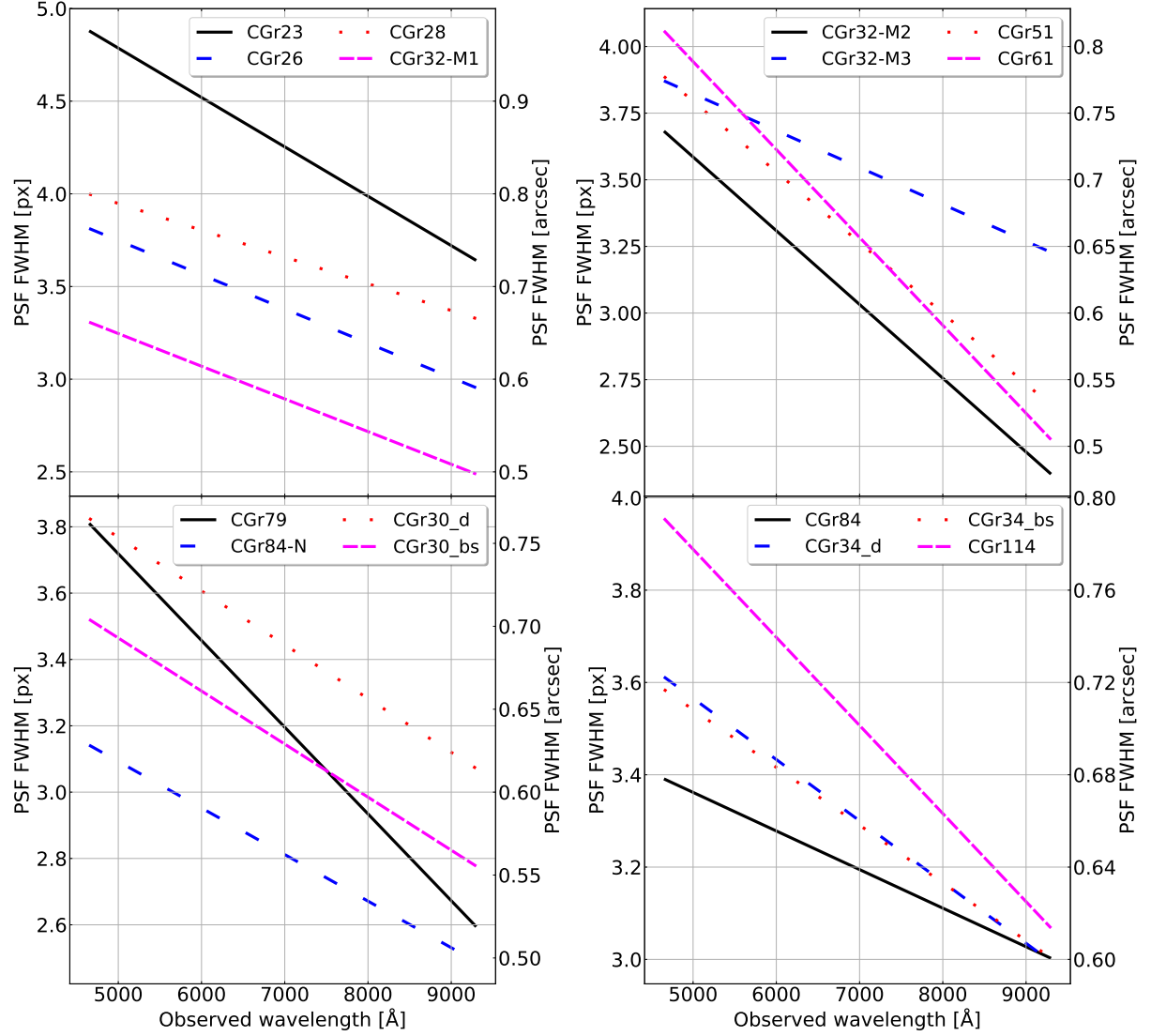


Figure 24: PSF FWHM variation with wavelength for the 16 MUSE fields (including *best_seeing* and *deep* observations) measured by V. Abril Melgajero and B. Epinat (LAM, Marseille). At least two values of the FWHM were derived from stars in the MUSE fields by fitting a Gaussian profile onto their light profile. We assumed a linear evolution with wavelength. Strong variations appear depending on the observed field.

B Additional information about kinematics

B.1 Velocity decomposition

MUSE velocity maps only give us the projected component of the 3D velocity field on the line of sight. This value is computed from the mean of the best fit Gaussian profile of the observed line, and from the Doppler shift formula

$$\frac{\lambda_{\text{obs}} - \lambda_{\text{em}}}{\lambda_{\text{em}}} = \frac{v}{c} \quad (27)$$

with v positive if it recedes from us and negative if it approaches. This means the only measure we have is the radial component of the gas velocity within the pixels. If we use the same coordinate system as defined in Epinat et al. (2008), we can write the observed projected radial component V_{obs} as

$$V_{\text{obs}}((x_c, y_c), R, \theta, i, V_{\text{sys}}, \text{PA}) = V_{\text{sys}} + [V_{\text{rot}}(R) \cos \theta + V_{\text{exp}}(R) \sin \theta] \sin i + V_z(R) \cos i \quad (28)$$

where (x_c, y_c) is the galaxy centre position, R the radial distance in the galactic plane, i the galaxy inclination and PA the kinematical position angle (which might be different from the morphological one). In Eq. 28, the velocity components are (a) V_{sys} the systematic velocity (b) V_{rot} the rotational velocity tangent to the plane of the galaxy (c) V_{exp} the expansion velocity oriented in the radial direction in the galactic plane (d) V_z the vertical component normal to the plane. The dependence on the kinematical PA is implicit since θ is defined as the angle in the galactic plane counted from the major axis. Thus, $\theta = 0^\circ$ (90°) when we measure the velocity of a point on the major (minor) axis. The dependence on the galaxy centre position is also implicit as the radial distance is computed relative to this point.

Both R and θ can be easily derived given (x_c, y_c) and the PA, but the inclination of the galaxy must be known in advance. Indeed, models tend to poorly converge when the inclination is let free to vary. More importantly, assuming the rotation curve along the major axis reaches a maximum rotational velocity or at least a plateau, we deduce from Eq. 28 that the maximum rotational velocity will scale as

$$V_{\text{obs}}^{\text{max}}(R_{\text{max}}, i) = V_{\text{rot}}(R_{\text{max}}) \sin i \quad (29)$$

where R_{max} represents the radius where the maximum/plateau velocity is reached. Thus, just by looking at the rotation curve and by measuring its maximum value, we cannot raise the degeneracy between the inclination, which will lower the velocity, and the real maximum rotational velocity. Hence, it must be used as a fixed input.

B.2 Computing the disk scale length

The model returns the minimum, maximum, average and median values for the dispersion map once corrected of beam smearing effects. We also recover the rotation velocity on the plateau

V_c , as well as the radius at which it is reached R_c and the maximum radius where the fit was performed R_{last} .

We compute the maximum velocity at $2.2R_d$, with R_d the disc scale length. This is defined as the radial distance in a morphological exponential disc model where the intensity drops by a factor of e with respect to the central value. From this definition, we can compute its scaling relation with $R_{1/2}$. From Eq. 2 and given that $I(R_d) = I_0 e^{-1} = I_e e^{-b_1(R_d/R_e - 1)}$, we find

$$R_e = b_1 R_d \quad (30)$$

where b_1 is the solution of the equation $2\gamma(2, b_1) = \Gamma(2)$. This also translates as

$$\int_0^{b_1} t e^{-t} dt = 1 - e^{-b_1}(1 + b_1) = 1/2 \quad (31)$$

for which we find a solution by making the substitution $b_1 \rightarrow -y - 1$ and using the Lambert W function

$$b_1 = -W\left(-\frac{1}{2e}\right) - 1 \approx 1.67835 \quad (32)$$

where we only kept the positive, physically meaningful solution.

C Additional plots for the analysis

C.1 TFR

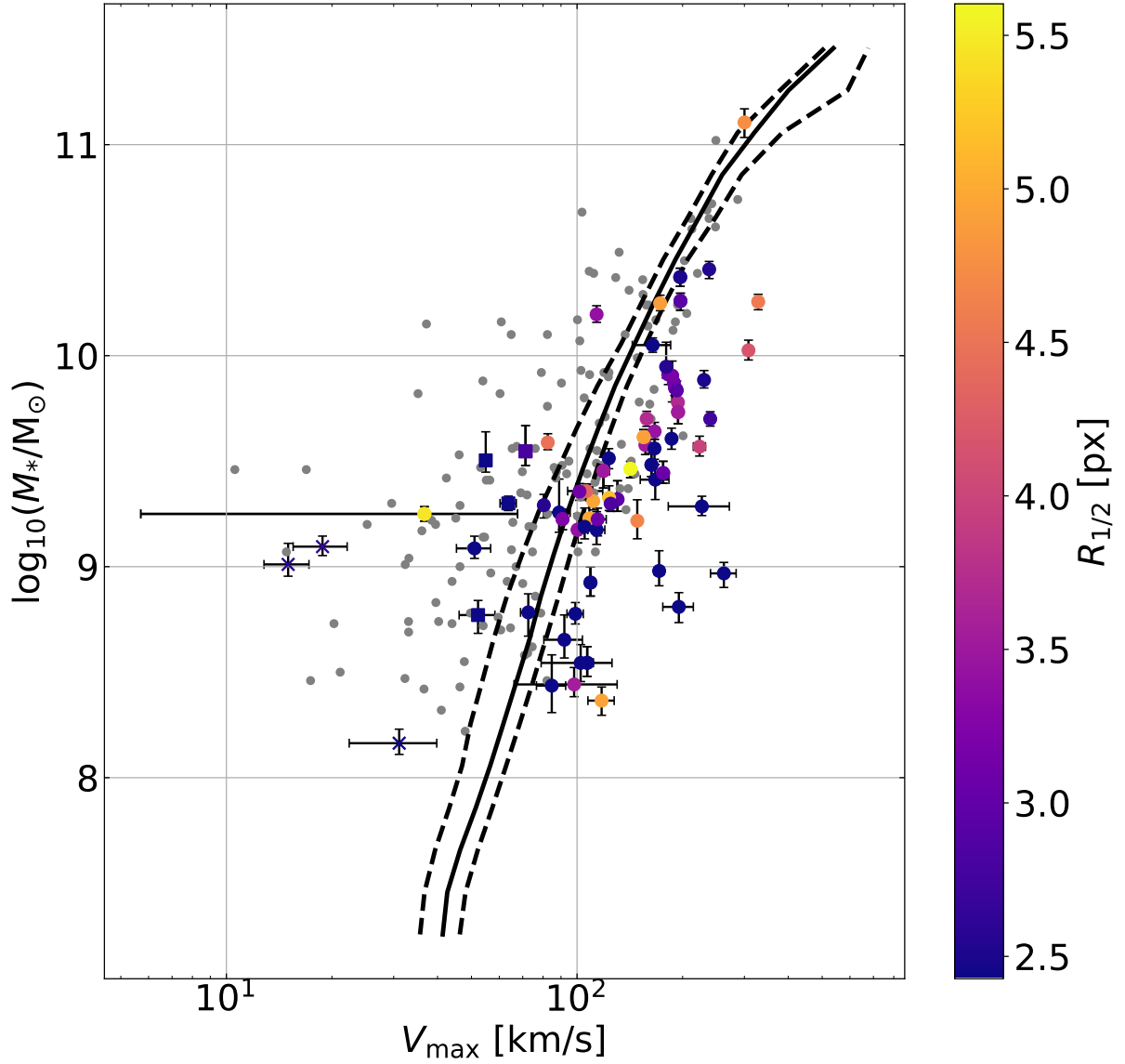


Figure 25: Same plot as in Fig. 20 but colour coded according to the apparent angular size (half-light radius) on the sky. The legend is similar to that in Fig. 20. As for redshift, we do not find a significant evolution, though all the dispersion dominated galaxies with low V_{max} are also found to have the lowest sizes, which is in agreement with the results shown in Fig. 19.

C.2 Effect of the inclination on the TFR

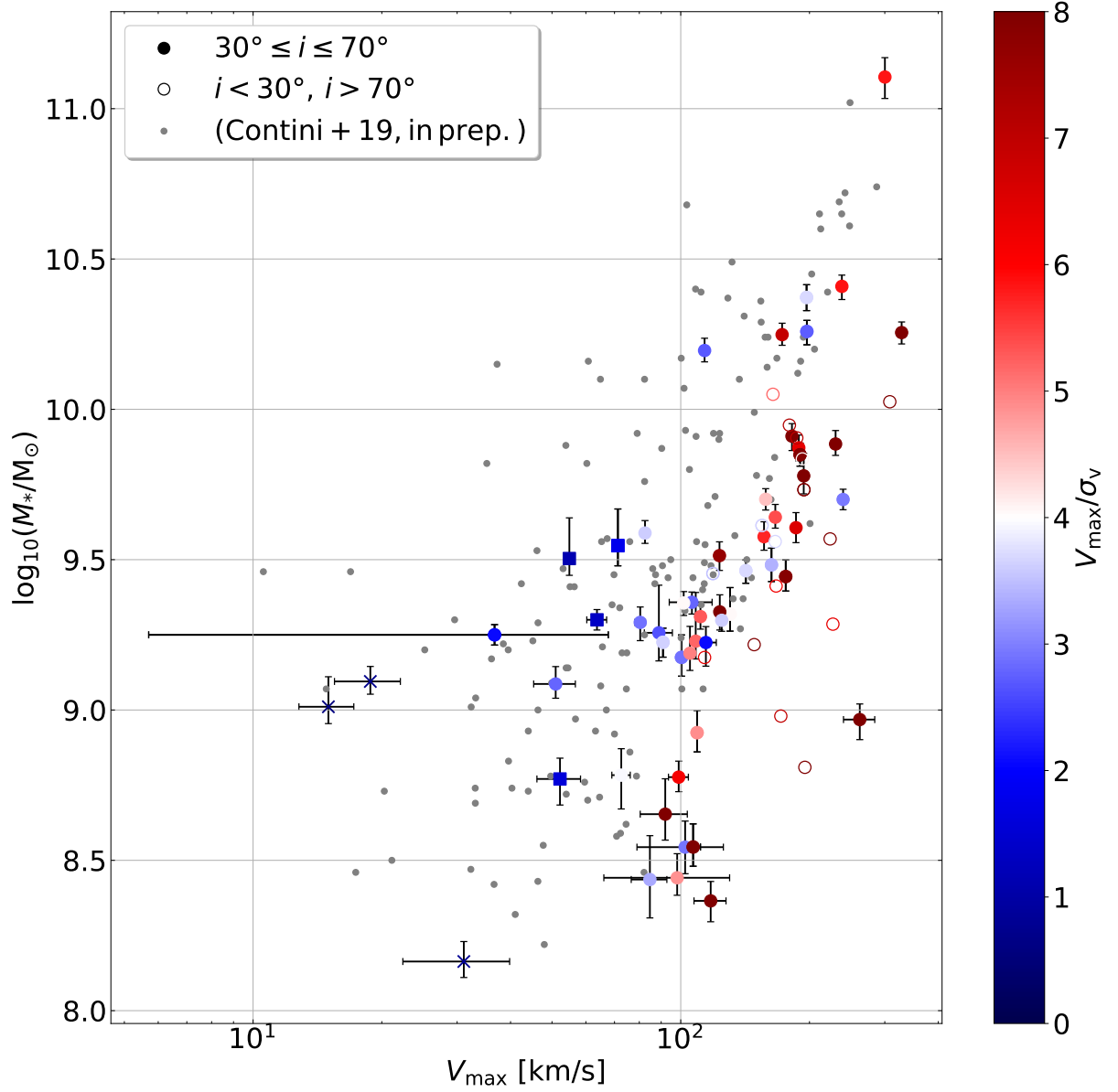


Figure 26: Tully-Fisher Relation for galaxies with a reasonable inclination $30^\circ \leq i \leq 70^\circ$ (filled circles with error bars) compared against face-on ($i < 30^\circ$) and edge-on ($i > 70^\circ$) galaxies.

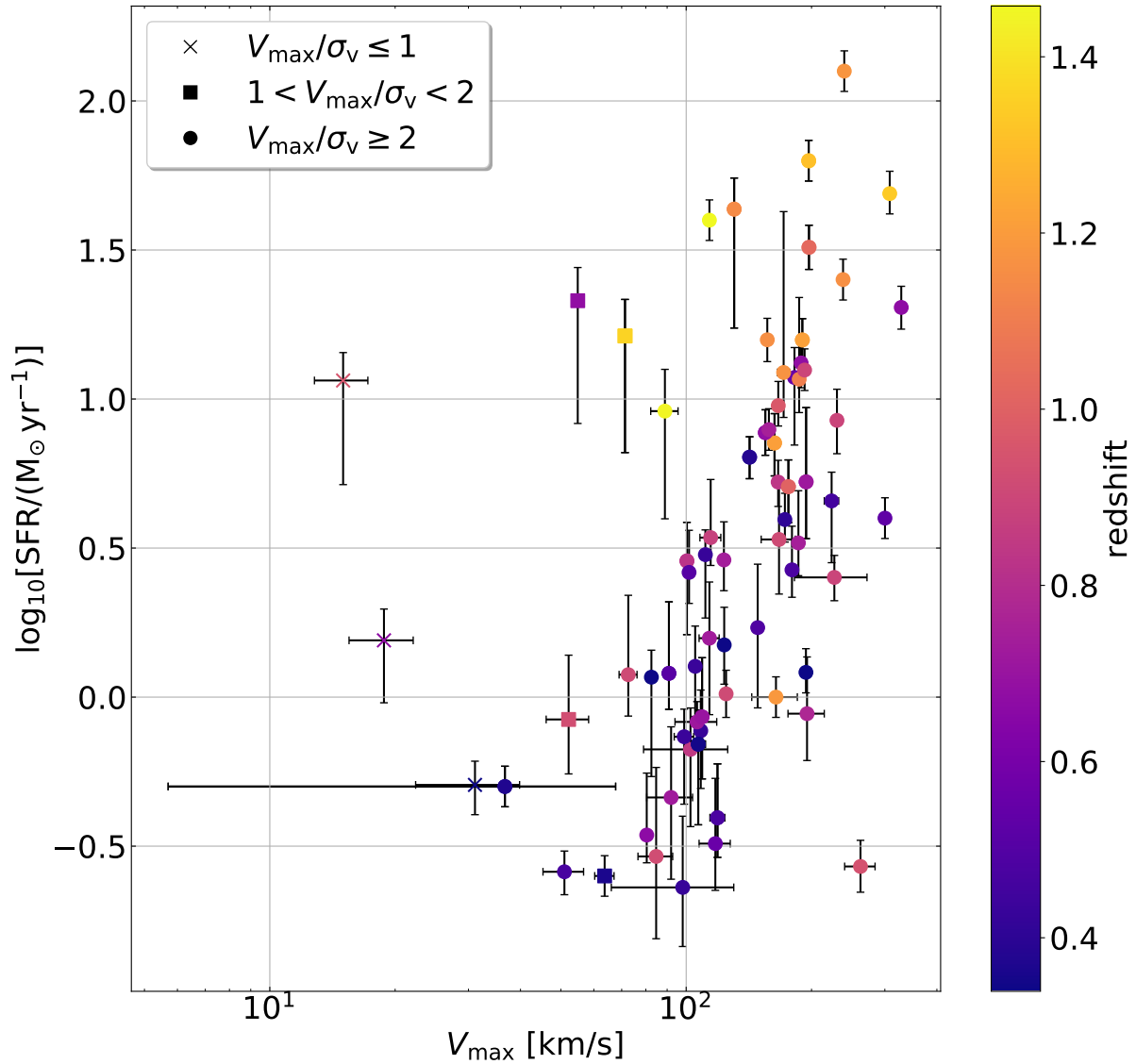
C.3 SFR – V_{\max} relation

Figure 27: $\log_{10} \text{SFR} - \log_{10} V_{\max}$ diagram with galaxies colour coded according to their redshift. We find a link between the SFR and the maximum rotation velocity. This is consistent with the galaxies main-sequence shown in Fig. 15 and with the TFR in Fig. 20.

D Morpho-kinematics parameters of the sample

Galaxy ¹ ID	z ²	$\log_{10} \text{SFR}$ ³ ($\text{M}_{\odot} \text{yr}^{-1}$)	$\log_{10} M_{*}$ ⁴ (M_{\odot})	$R_{1/2}$ ⁵ (")	R_c ⁶ (px)	V_c ⁷ (km/s)	σ_v ⁸ (km/s)	χ^2 ⁹
114_21	0.345	+0.0	8.16	7.65	5.1	59.9	13.5	0.68
114_79	0.423	+0.5	9.31	4.95	6.5	111.2	21.0	1.37
114_99	0.423	-0.1	9.23	4.97	4.1	108.4	20.8	2.74
114_104	0.539	-0.3	9.45	1.79	6.9	116.2	21.4	0.63
114_46	0.924	-0.5	8.44	1.78	1.0	84.7	25.5	0.73
23_13	0.677	+1.3	9.5	1.81	1.0	54.9	48.3	2.41
23_19	0.953	+1.1	9.01	2.57	1.0	15.0	26.4	0.59
23_25	0.677	+1.0	10.04	3.48	8.8	217.4	42.5	2.14
23_30	0.676	+1.1	9.87	3.15	1.0	188.8	29.5	4.22
23_90	0.379	-0.8	8.52	4.07	6.6	79.6	6.3	0.44
23_94	0.941	-0.6	8.97	2.04	4.1	262.2	4.5	0.85
23_120	1.159	+1.2	9.58	3.51	1.0	156.6	27.5	4.40
23_110	0.731	+0.2	9.17	2.43	1.0	113.7	17.7	0.86
26_59	0.826	+0.1	9.16	2.37	8.0	169.8	24.6	0.60
26_87	1.333	+1.7	10.03	4.17	5.1	308.2	20.8	15.03
26_136	1.188	+0.0	10.05	2.39	1.8	164.3	31.4	0.99
26_5	0.533	+0.6	11.11	4.75	1.0	300.2	51.6	3.66
26_31	0.562	-0.5	8.37	4.93	1.0	117.5	10.9	1.20
26_41	0.531	+0.4	9.36	1.81	9.0	315.0	44.7	0.59
26_71	0.967	+1.0	9.64	3.45	2.1	166.4	30.8	1.94
26_102	0.554	+1.1	9.91	3.12	1.0	182.0	20.3	3.83
26_128	0.425	-0.6	8.44	3.56	3.1	98.1	20.2	0.78
28_4	0.718	-0.1	9.36	4.34	3.9	106.2	37.8	1.44
28_5	0.874	+0.5	9.22	3.09	2.5	114.5	55.0	1.85
28_15	1.181	+2.1	9.7	2.75	1.0	239.7	81.6	4.64
28_37	0.894	+0.9	9.88	2.5	1.0	230.2	22.8	2.39
28_44	0.363	-0.6	9.3	2.28	1.0	63.7	46.9	1.44
28_55	0.894	+0.4	9.29	1.91	2.9	226.9	35.7	0.94
28_59	0.737	+0.5	9.51	1.92	1.0	123.2	16.1	0.75
28_83	0.719	-0.4	8.31	2.05	7.2	54.0	24.5	1.15
30_d_45	1.211	+0.9	9.48	2.4	6.3	163.0	48.1	2.42
30_d_67	0.381	+0.8	9.46	5.6	5.2	142.0	38.5	1.49

Table 2: Table of morphological and kinematical parameters for the sample of selected field galaxies. 1. Galaxy ID with first the COSMOS group number and then the galaxy number, 2. redshift, 3. Star Formation Rate, 4. Stellar mass, 5. Half-light radius, 6. Turnover radius (MUSE pixel), 7. Plateau velocity, 8. Velocity dispersion, 9. Reduced χ^2 .

Galaxy ¹ ID	z ²	$\log_{10} \text{SFR}$ ³ ($M_{\odot} \text{ yr}^{-1}$)	$\log_{10} M_{*}$ ⁴ (M_{\odot})	$R_{1/2}$ ⁵ (")	R_c ⁸ (px)	V_c ⁹ (km/s)	σ_v ¹⁰ (km/s)	χ^2 ¹¹
30_d_77	0.478	-0.4	9.45	3.51	4.7	118.9	33.7	0.72
30_d_79	0.828	+0.5	9.17	3.42	0.9	100.4	34.8	1.68
30_d_91	0.682	+0.9	9.61	4.91	5.6	154.9	42.4	2.13
30_d_108	1.19	+1.1	9.73	1.87	8.3	114.5	34.9	1.04
30_d_146	1.144	+1.6	9.32	2.96	0.9	130.4	32.2	6.74
30_d_148	0.373	-0.3	9.25	5.45	14.1	36.7	17.6	1.15
30_d_154	1.216	+1.2	9.85	3.14	0.9	190.1	24.0	4.34
30_d_27	1.361	+1.2	9.55	2.8	0.9	71.3	39.7	0.62
30_d_139	0.701	-0.1	8.92	2.39	1.0	109.2	22.3	1.40
32-M1_375	0.342	-0.0	8.7	2.94	11.5	242.3	5.3	0.29
32-M1_429	1.104	+1.1	9.91	3.18	0.8	186.8	26.6	3.42
32-M1_431	0.377	-1.2	8.37	1.76	4.2	37.5	9.5	0.39
32-M1_455	0.55	+0.6	10.11	3.43	15.5	216.6	39.9	1.31
32-M1_376	0.914	+0.5	9.41	1.92	1.6	167.1	26.9	0.73
32-M1_414	0.847	-0.2	8.54	2.12	4.4	102.4	34.9	1.30
32-M2_209	0.49	+0.2	9.22	4.66	1.0	148.5	14.2	2.85
32-M2_216	0.455	+0.7	9.57	3.98	5.0	223.5	27.9	1.45
32-M2_232	0.321	+0.2	9.33	5.17	8.7	123.4	12.6	5.02
32-M2_309	0.833	+0.7	9.56	2.2	0.9	166.3	45.1	1.83
32-M2_154	1.445	+1.0	9.26	1.92	4.1	88.9	33.6	0.93
32-M3_32	0.476	+0.4	9.95	2.56	3.3	179.5	24.9	1.14
32-M3_196	0.322	+0.1	9.78	3.7	5.5	193.9	23.8	2.63
34_d_25	0.717	+0.7	9.73	3.54	3.0	194.1	20.2	3.74
34_d_50	0.514	+0.1	9.23	3.25	2.0	90.9	24.9	1.58
34_d_90	0.306	-0.9	8.76	3.01	7.9	115.5	4.6	0.64
34_d_103	0.348	-0.2	8.54	2.31	4.4	106.9	11.7	1.83
34_d_123	1.006	+0.7	9.44	3.05	5.2	176.0	22.3	3.57
34_d_144	0.321	-0.8	8.07	2.99	15.5	359.3	38.6	0.82
34_d_154	1.305	+1.8	10.37	2.51	7.5	196.9	53.2	3.22
34_d_155	1.027	+1.5	10.26	2.94	2.9	197.2	72.5	11.44
34_d_17	1.026	+0.1	8.77	1.97	3.8	172.2	25.2	2.29
51_28	0.7	+0.7	9.33	2.24	11.2	218.7	23.1	5.12
51_123	1.245	+1.0	9.96	1.79	6.1	205.8	50.0	0.76
51_23	0.925	-0.1	8.77	2.0	0.9	52.2	33.1	0.96
51_49	0.912	+0.1	8.78	2.15	0.9	72.6	18.4	0.52
51_77	0.727	-0.3	8.65	2.11	1.0	92.0	10.4	3.64
61_7	1.172	+1.1	8.98	2.43	3.0	171.4	24.6	4.59
61_12	0.339	-0.3	8.16	2.43	1.0	31.1	37.4	1.65
61_25	0.329	+0.1	9.59	4.48	1.0	82.5	22.8	1.20
61_39	0.432	+0.1	9.19	2.39	1.0	105.1	21.1	0.99
61_87	1.163	+1.4	10.41	2.53	0.9	238.1	40.6	2.69
61_102	0.465	-0.4	8.85	1.89	15.5	115.6	11.4	0.89
61_117	0.599	-0.3	8.56	3.14	7.2	193.9	14.9	0.68
61_79	0.883	+0.1	8.82	2.16	15.2	670.7	22.7	0.41
79_41	0.749	+0.9	9.7	3.72	3.4	158.0	35.2	9.12
79_42	1.458	+1.6	10.2	3.42	0.8	113.7	42.2	15.16
79_51	0.912	+0.0	9.3	2.82	3.7	124.7	34.5	12.04

Table 3: Table of morphological and kinematical parameters: part II. Description is similar to Table 2

Galaxy ¹ ID	z ²	$\log_{10} \text{SFR}$ ³ ($M_{\odot} \text{ yr}^{-1}$)	$\log_{10} M_{*}$ ⁴ (M_{\odot})	$R_{1/2}$ ⁵ ($''$)	R_c ⁸ (px)	V_c ⁹ (km/s)	σ_v ¹⁰ (km/s)	χ^2 ¹¹
79_80	0.743	+0.5	9.61	2.1	3.0	186.0	28.4	2.58
79_112	0.433	−0.1	8.78	2.22	2.6	98.9	16.1	0.85
79_114	0.668	+1.3	10.26	4.56	9.4	328.5	29.0	33.56
79_120	0.896	+1.1	9.84	2.92	2.6	192.5	47.1	4.91
79_69	0.668	−0.1	8.54	2.58	15.5	165.6	19.9	0.23
84-N_8	0.407	+0.6	10.25	4.89	5.1	172.6	24.9	1.70
84-N_20	0.668	+0.9	9.8	3.0	7.2	135.3	20.2	0.92
84-N_21	0.669	+0.2	9.09	2.65	0.9	18.8	25.4	0.78
84-N_66	0.773	−0.1	8.81	2.4	4.0	195.1	20.8	0.82
84_39	0.665	−0.5	9.29	2.56	1.0	80.4	27.7	0.91
84_54	0.506	+0.4	9.36	3.11	3.5	101.6	25.1	2.13
84_132	0.471	−0.6	9.09	1.94	3.4	51.0	18.2	1.02
84_146	0.747	+0.7	9.41	3.41	13.2	450.0	24.2	2.85
84_98	0.444	−0.9	9.06	16.04	8.4	117.7	14.2	0.45

Table 4: Table of morphological and kinematical parameters: part III. Description is simliar to Table 2